minerals

MDPI

Article

Magmatic–Hydrothermal Transport of Metals at Arc Plutonic Roots: Insights from the Ildeus Mafic–Ultramafic Complex, Stanovoy Suture Zone (Russian Far East)

Pavel Kepezhinskas [1,*], Nikolai Berdnikov [1], Nikita Kepezhinskas [2], Valeria Krutikova [1] and Ivan Astapov [1]

[1] Institute of Tectonics and Geophysics, Khabarovsk 680000, Russia; nick@itig.as.khb.ru (N.B.); nm32697@gmail.com (V.K.); astapov-itig@mail.ru (I.A.)
[2] APEX Geoscience Ltd., Edmonton, AB T5M 3Y7, Canada; kepezhinskasnp@outlook.com
* Correspondence: pavel_k7@yahoo.com

Abstract: The Ildeus mafic–ultramafic complex represents plutonic roots of a Triassic magmatic arc tectonically emplaced into the thickened uppermost crust beneath the Mesozoic Stanovoy collided margin. The mafic–ultramafic complex cumulates host Ni-Co-Cu-Pt-Ag-Au sulfide-native metal-alloy mineralization produced through magmatic differentiation of subduction-related primary mafic melt. This melt was sourced in the metal-rich sub-arc mantle wedge hybridized by reduced high-temperature H-S-Cl fluids and slab/sediment-derived siliceous melts carrying significant amounts of Pt, W, Au, Ag, Cu and Zn. Plutonic rocks experienced a pervasive later-stage metasomatic upgrade of the primary sulfide–native metal–alloy assemblage in the presence of oxidized hydrothermal fluid enriched in sulfate and chlorine. The new metasomatic assemblage formed in a shallow epithermal environment in the collided crust includes native gold, Ag-Au, Cu-Ag and Cu-Ag-Au alloys, heazlewoodite, digenite, chalcocite, cassiterite, galena, sphalerite, acanthite, composite Cu-Zn-Pb-Fe sulfides, Sb-As-Se sulfosalts and Pb-Ag tellurides. A two-stage model for magmatic–hydrothermal transport of some siderophile (W, Pt, Au) and chalcophile (Cu, Zn, Ag) metals in subduction–collision environments is proposed.

Keywords: arc plutonic roots; Mesozoic Stanovoy collided margin; ultramafic metasome; sediment melting; adakites; hydrothermal fluids; Ni-Co-Cu-Pb-Zn sulfides; native ore metals and alloys; magmatic–hydrothermal transport

Citation: Kepezhinskas, P.; Berdnikov, N.; Kepezhinskas, N.; Krutikova, V.; Astapov, I. Magmatic–Hydrothermal Transport of Metals at Arc Plutonic Roots: Insights from the Ildeus Mafic–Ultramafic Complex, Stanovoy Suture Zone (Russian Far East). *Minerals* **2023**, *13*, 878. https://doi.org/10.3390/min13070878

Academic Editor: Federica Zaccarini

Received: 18 May 2023
Revised: 15 June 2023
Accepted: 27 June 2023
Published: 29 June 2023

1. Introduction

Most ore deposits at modern and ancient convergent margins are formed from metals contributed by asthenospheric and lithospheric mantle sources [1–9]. However, the exact modes of metal transport in subduction zone environments are still subject to vigorous scientific debate. The predominant paradigm suggests that ore metals are preferably transported by dense hydrous fluids associated with magma movement between a range of mantle and crustal geochemical reservoirs [10–26]. Most siderophile and chalcophile elements eagerly partition into an aqueous fluid phase, especially in the presence of sulfur and halogens [27–38]. The transport and mobilization of ore elements can also be assisted by the formation of metal-rich sulfide magma [39–45]; pulsated build-up of large, fluid-saturated sub-volcanic magma chambers [46–52]; or by flotation of metal-rich sulfides and other ore minerals (e.g., magnetite) on gaseous bubbles in lava flows and shallow melt conduits [53–59]. Recent discoveries of native metals (Cu, Ag, Au) and Cu-Sn-Co-Ag alloys in vesicular basalts from Hawaii, Vesuvius, Etna and Stromboli suggest metal pre-concentration and enrichment via vapor-assisted fractional crystallization during lava solidification prior to later-stage hydrothermal alteration and the remobilization of ore metal components [60,61].

We have recently reported textural and compositional evidence for the association of Au, Au-Ag and Cu-Ag-Au alloys as well as other chalcophile and siderophile metals with magmatic minerals in a range of explosive volcanic rocks from the Lesser Khingan Range in the Russian Far East, Cretaceous adakite lavas from the Stanovoy Suture Zone in East Siberia, Tertiary shoshonite from the Western United States and young dacitic lava from the Bolivian Andes [62–65]. These data suggest high-temperature magmatic origins for some ore components in subduction tectonic settings (including possible slab failure and breakoff cases) and the cycling of ore metals in the crust–mantle system through the percolation of metal-rich, fluid-saturated mantle-derived sulfide and silicate liquids [66–68]. In addition, arc-related plutonic root systems provide effective pathways for metal transport from lithospheric and asthenospheric mantle sources to the upper crust [69,70], whereupon these metals are chemically and physically transformed and incorporated under predominantly oxidized conditions into various hydrothermal deposits at convergent and collided margins [9,13,71–74].

This paper presents new geological, mineralogical and geochemical data from the recent (2022) drilling of a mineralized arc-related plutonic system in the Stanovoy Suture Zone (SSZ) of the Russian Far East, which casts new light on ore metal transport and mobility in subduction zones [69,70]. We specifically aim to address the following issues: (1) the diversity of metal associations in arc-related plutonic systems; (2) the relative role and importance of magmatic versus hydrothermal processes; and (3) the composition and evolution of fluid and redox conditions during the formation and development of magmatic plumbing systems at ancient convergent and collided margins.

2. Geologic Background and Samples

The Stanovoy Suture Zone (SSZ) forms the northernmost part of the Central Asian Orogenic Belt (CAOB) at its junction with the southern edge of the Siberian craton (Figure 1A). The CAOB represents the world's largest accretionary orogen with a substantial Phanerozoic juvenile crustal component [75,76]. It is composed of Proterozoic to Paleozoic oceanic, island-arc, back-arc basin, seamount and oceanic plateau terranes tectonically mingled with fragments of the Precambrian structural–metamorphic basement [75–77] and stitched together by granitoid complexes [78]. The SSZ includes variably metamorphosed (mostly under amphibolite, locally granulite facies conditions) Precambrian to Phanerozoic continental, oceanic and arc-related terranes thrusted onto the southern margin of the Siberian craton (Aldan shield) during closure of the Mongol–Okhotsk oceanic basin in the Early Mesozoic [79,80]. The modern structure of the SSZ is clearly reminiscent of a typical collisional orogen affected on the regional scale by post-collisional extensional tectonics and mafic-to-felsic magmatism [69,81].

The central part of the SSZ is composed of several Phanerozoic-arc-related terranes tectonically intermingled with Precambrian high-grade metamorphic rocks intruded by Mesozoic mafic–ultramafic complexes, some of which are quite intricately constructed with a complex magmatic crustal architecture [69]. These mafic–ultramafic complexes are interpreted as plutonic roots of a Mesozoic magmatic arc (similar to the modern Andes and Kamchatka) formed in response to the northward subduction of the Mongol–Okhotsk oceanic floor beneath the Siberian craton [82]. The Triassic (232–233 Ma) Ildeus mafic–ultramafic complex intrudes Precambrian gneisses, mafic crystalline schists and amphibolites of the Precambrian Stanovoy Series and carries recently (2018–2022) discovered exotic Ni-Co-Cu-Au-Ag-Pt sulfide-native metal-alloy mineralization hosted in cumulate and metasomatic ultramafic rock lithologies [69,70,83]. Mineralized ultramafic rocks are associated with a distinctive magnetic signature (Figure 1B) coupled with low apparent resistivity and elevated polarization values usually coincident with the highest abundances of sulfides, native metals and alloys in ultramafic plutonic rock.

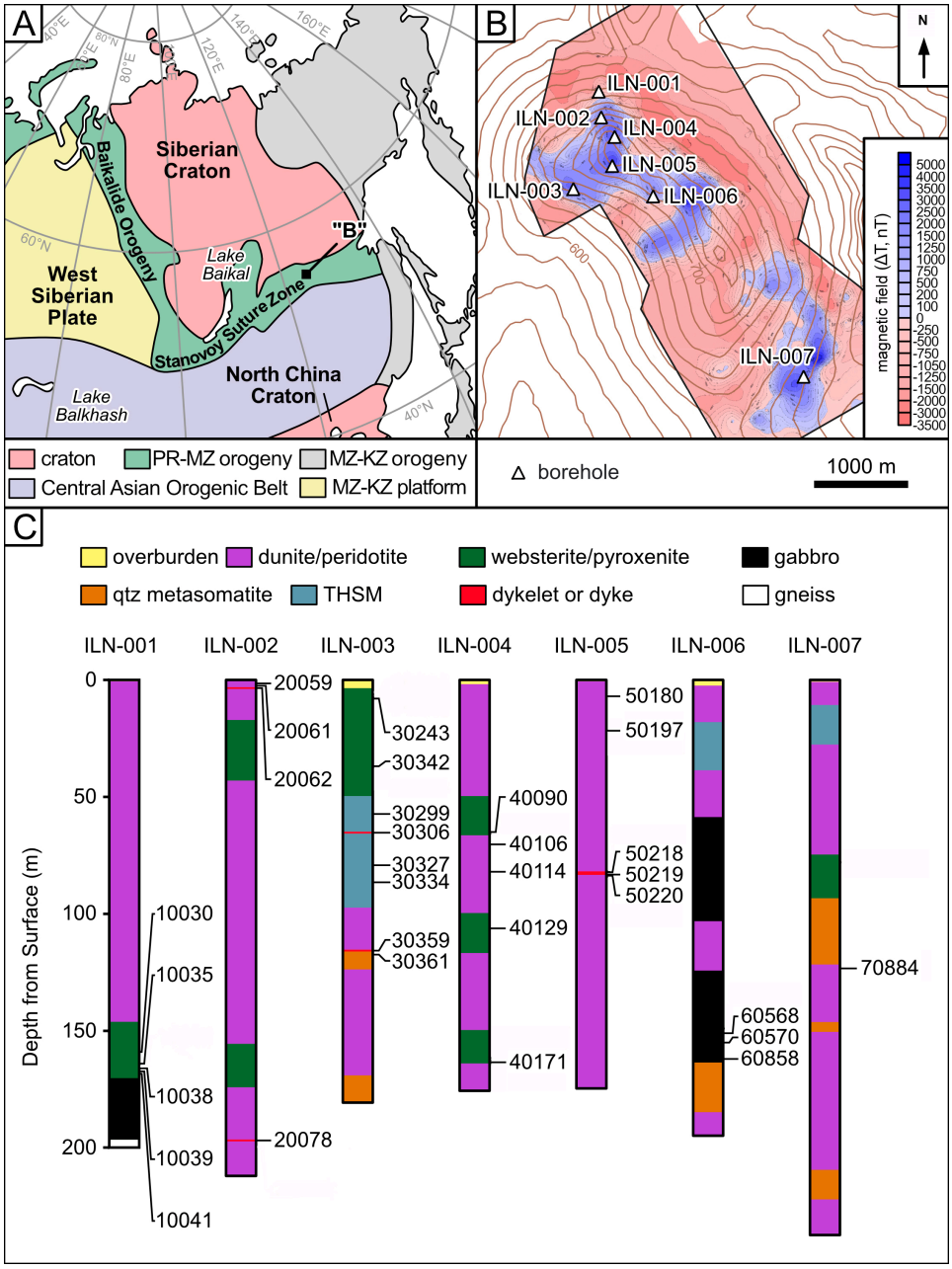

Figure 1. (**A**) Simplified tectonic setting of the Stanovoy Suture Zone (SSZ) in the general geodynamic context of Eastern Siberia and Far East Russia. "B"—location of the Ildeus complex. (**B**) Magnetic map of the northern portion of Ildeus mafic–ultramafic complex showing location of the 2022 drill holes. (**C**) Lithologic columns for the northern portion of the Ildeus complex based on the 2022 drilling results.

The Ildeus intrusion is characterized by crude lithological zoning (Figure 1C) with its core being predominantly composed of various ultramafic rocks such as dunite, plagioclase-bearing dunite, harzburgite, lherzolite, olivine websterite and wehrlite. Relatively narrow (<50 m) marginal zones are composed of gabbro-norite (locally grading into norite) and gabbro-anorthosite. Contacts with host Precambrian gneiss based on field mapping are almost always tectonic. However, hole ILN-001 intersected an intrusive contact between the fine-grained gabbro-norite and amphibole-biotite gneiss (Figure 1C). Some parts of the Ildeus complex are characterized by large-scale primary magmatic layering (holes ILN-002 and ILN-006 in Figure 1C). The ultramafic sequence is frequently intruded by pyroxenite

and lamprophyre dikes along with felsic veins and dikelets (Figure 2). Felsic veins (Figure 2) display very high Sr/Y ratios (>100) typical of high-SiO_2, low-MgO adakites [64,84]. High-Ti and Nb (TiO_2 = 3–3.5 wt.%; Nb = 10–15 ppm) lamprophyres [69] are similar to arc-related high-Nb basalts associated with the subduction of young oceanic crust, adakite-mantle hybridization and the melting of rutile/titanite-rich mantle sources in subduction and collision environments [64,85,86].

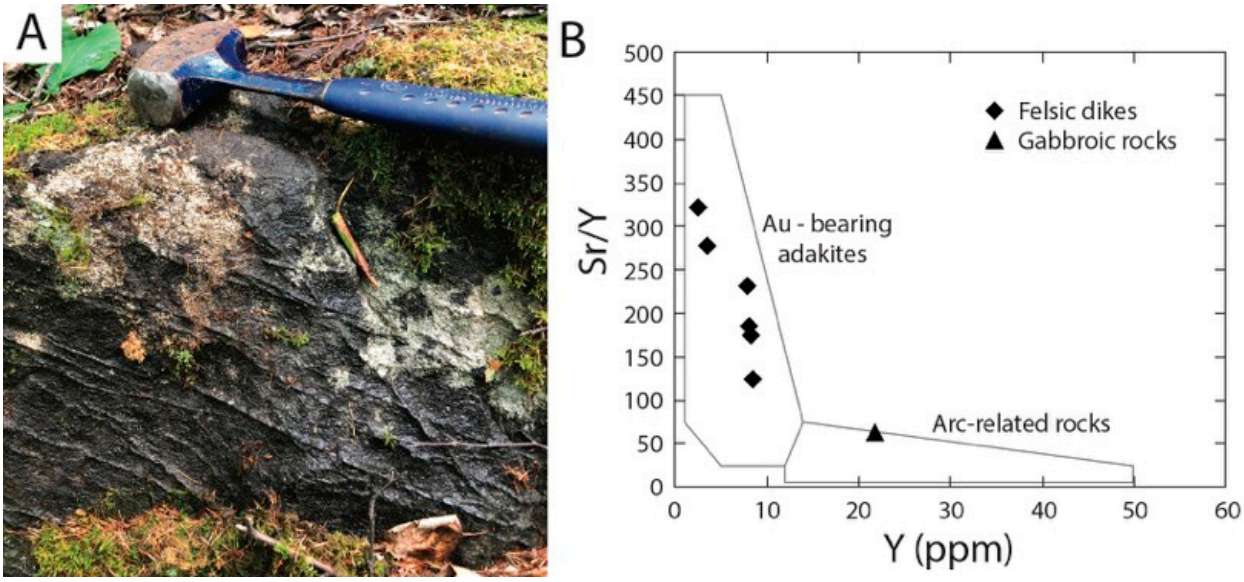

Figure 2. (**A**) Field occurrence of felsic veins in Ildeus ultramafic rock. (**B**) Sr/Y versus Y (ppm) discrimination diagram for felsic veins and gabbroic rocks from the Ildeus intrusion. Fields for Au-bearing adakites and arc-related igneous rocks are modified from [84,85].

Mafic–ultramafic plutonic rocks from the Ildeus complex have been overprinted with two principal types of the later-stage hydrothermal alteration: (1) hydrous ultramafic and (2) silicic (Figure 1C). Ultramafic metasomatic rocks are typically composed of talc, serpentine and chlorite with minor carbonate and tremolite (with some relics of primary magmatic pyroxene and olivine). They commonly form either stockwork zones 20–50 m in width, or narrow (typically under 10 m) ultramafic metasomes with completely obliterated igneous textures and primary mineral assemblages. Quartz-rich (silicic) metasomes are frequently associated with low- and high-sulfidation quartz veins with minor calcite, adularia and mica and are occasionally developed around adakite dikes and veins (Figure 3F). Silicic metasomatic zones are principally composed of quartz with minor and variable amounts of biotite, muscovite, calcite, adularia, barite and some (usually under 5 tmodal percent) sulfide represented by pyrite, pyrrhotite, chalcopyrite, sphalerite, galena and tennantite-tetrahedrite. Relic, chemically and physically corroded and abraded pentlandite and Co-rich pentlandite are also occasionally observed among silicic metasomatic assemblages. Locally, narrow zones (first meters) of silicic metasomes and quartz veins crosscut ultramafic hydrothermal assemblages (talc + serpentine + chlorite), indicating that silicic alteration (including isolated quartz veinlets and bulk silicification) was the latest metasomatic episode within the Ildeus magmatic–hydrothermal system.

Samples of all ultramafic and mafic igneous lithologies along with ultramafic metasomes and felsic veins were collected from the 2022 diamond drill core (Figure 3). Relative positions of all samples used in this study within the individual lithologic drill hole columns are shown in Figure 1C. Igneous and metasomatic rocks as well as the associated mineralization were studied using a range of petrologic and geochemical methods.

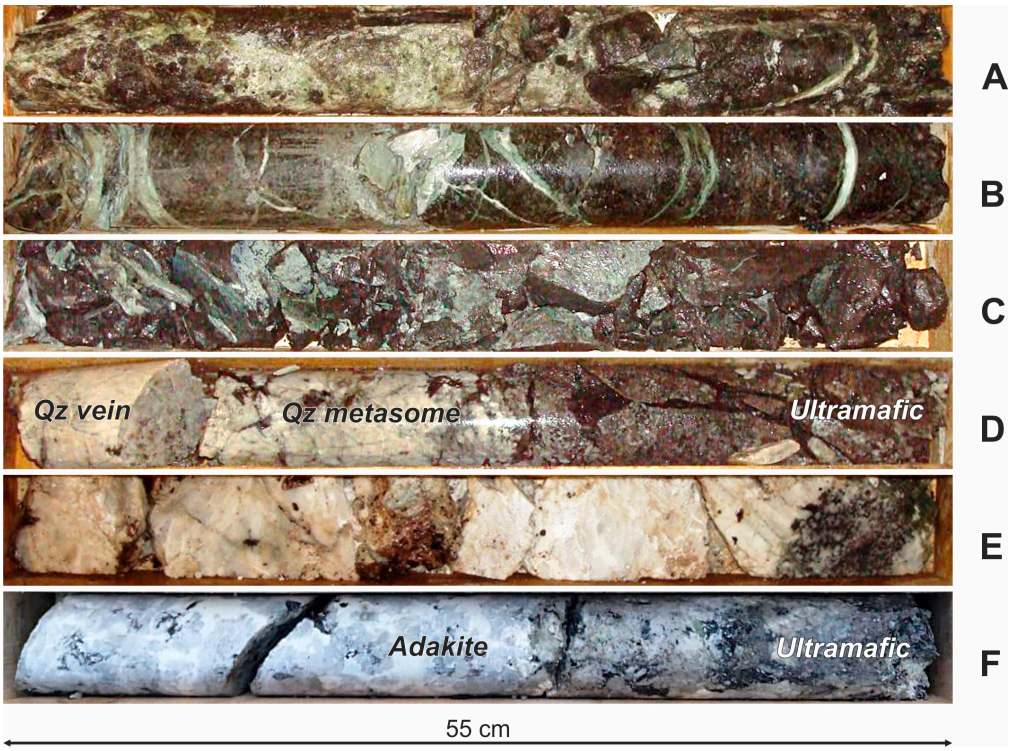

Figure 3. Metasomatic rocks and later-stage felsic dikes in the Ildeus mafic–ultramafic complex. (**A**) Ultramafic (talc + chlorite + serpentine ± carbonate) metasome in harzburgite. (**B**) Ultramafic (talc + serpentine ± chlorite ± carbonate) stockwork in dunite. (**C**) Spotty chloritization around ultramafic metasomes. (**D**) Quartz-rich (with minor calcite, adularia, chlorite, biotite, sericite and muscovite) metasome in contact with quartz vein (on the left) and ultramafic rock (on the right). (**E**) Quartz-rich (with minor calcite, adularia, chlorite, biotite, sericite and muscovite) metasome with relics of host ultramafic rock. (**F**) Adakite dike intruding ultramafic rock.

3. Analytical Methods

Petrographic studies of magmatic and metasomatic rocks were carried out using an Imager A2m petrographic microscope (Carl Zeiss, Oberkochen, Germany).

Major element oxides in magmatic and metasomatic rocks from the Ildeus mafic–ultramafic complex were measured on pressed pellets using a S4 Pioneer XRF spectrometer (Bruker, Leipzig, Germany). The analytical accuracy for major element oxides in the course of this study was ± 10%. Abundances of trace elements were determined with an ELAN 9000 ICP-MS (Perkin Elmer, Woodbridge, Ontario, Canada) after the acid digestion of a powdered sample. International geochemical reference samples LDI-3 (gabbro), WMG-1a (mineralized gabbro), BHVO-2 (USGS; Hawaiian basalt) and JB-3 (Geological Survey of Japan; Fuji basalt), along with Perkin Elmer standard solutions PE# N9300231-9300234 for internal calibration, were used to control the accuracy of analytical measurements. In the course of this study, the accuracy was ±5% for trace element abundances of >20 ppm and ±10% for chemical elements with abundances of <20 ppm [70]. Platinum-group elements (Ru, Rh, Ir, Pd, Pt) and Au were determined by ICP-MS after separation and pre-concentration by Na_2O_2 fire-assay and tellurium co-precipitation following the method described in [87].

A detailed systematic study of native metals, alloys and associated mineral phases was completed using a VEGA 3 LMH TESCAN (Czech Republic) scanning electron microscope (SEM) with the Oxford X-Max 80 Gb energy-dispersive spectrometer (EDS) with the following operating conditions: accelerating voltage of 20 kV, beam current of 530 nA and beam diameter of 0.2 μm. A set of reference samples including 37 natural and synthetic oxides, minerals and pure native metals (Oxford/108699 no. 6067) was used as standards.

Co-standard Oxford Instruments/143100 no. 9864-15 was used for daily calibration of the SEM instrument. The accuracy of the EDS analyses was estimated to be ±0.1 wt.%. Special sample preparation protocols reported in detail in [68] designed to prevent contamination were utilized to expose metallic phases in situ and determine their relationships with host silicate and oxide phases as well as associated rock-forming and accessory minerals.

During the SEM-EDS analysis of micron-sized inclusions in silicate and oxide minerals, the area affected by X-ray radiation more often than not includes both the inclusion itself and a portion of host mineral (matrix) immediately surrounding the inclusion. Chemical elements present in the matrix are excited and added to the resultant X-ray energy spectrum of the micro-inclusion, making correct interpretation of the studied micro-object naturally challenging. We present in this paper results of X-ray analyses of micro-objects (micro-minerals, metals, alloys) screened and corrected for the energy peaks of matrix elements. The key principle of this screening procedure is to only account for elements not present in the composition of the matrix (host mineral). If the concentration of a certain element in the micro-inclusion is equal to the content of the same element in the surrounding matrix, this particular chemical element was treated as matrix-derived and excluded from any further consideration. We have also evaluated inter-element ratios in our SEM-EDS analyses of both host minerals and micro-inclusions. If inter-element ratios in both host and inclusion were identical or sufficiently similar, these chemical elements (or one of the analyzed elements) were interpreted as most probably host mineral-related and were excluded from the analytical results for a particular micro-inclusion. Matrix-screened and corrected metal contents in micro-inclusions were then normalized to 100%.

All analytical procedures were carried out at the Khabarovsk Innovative-Analytical Center (KhIAC) of the Institute of Tectonics and Geophysics, Far Eastern Branch of the Russian Academy of Sciences, Khabarovsk, Russian Federation.

4. Results

The results of the petrologic–geochemical investigation of magmatic and metasomatic rocks from the Ildeus mafic–ultramafic complex are presented in the following two sections. Major and trace element data for representative magmatic and metasomatic rocks from the Ildeus mafic–ultramafic complex are listed in Tables 1–4.

Table 1. Representative major and trace element compositions of peridotites.

Sample#	**20059**	**40114**	**50220**	**50180**	**50197**	**30361**	**40106**	**30327**	**50221**
Rock type	Dunite	Pl-Dunite	Pl-Dunite	Harz	Srp Harz	Harz	Lherz	Serp	Wehrlite
SiO_2 (wt.%)	42.30	40.22	39.19	49.52	41.70	42.38	50.02	38.77	42.49
TiO_2	0.05	0.17	0.08	0.19	0.17	0.25	0.33	0.35	0.19
Al_2O_3	1.85	4.67	3.69	3.41	3.11	2.72	4.16	7.53	5.92
Fe_2O_3	9.02	9.99	10.39	7.59	7.22	10.00	9.73	9.15	11.09
MnO	0.15	0.14	0.14	0.19	0.10	0.20	0.19	0.09	0.15
MgO	36.63	33.50	33.59	33.13	33.50	33.21	30.73	27.79	28.76
CaO	0.27	1.60	0.73	0.24	0.35	0.66	3.07	1.04	2.49
Na_2O	0.15	0.24	0.32	0.15	0.17	0.26	0.41	0.33	0.36
K_2O	0.01	0.07	0.06	0.02	0.01	0.34	0.05	0.55	0.60
P_2O_5	0.02	0.03	0.02	0.01	0.02	0.04	0.02	0.03	0.02
LOI	11.15	10.26	12.89	6.20	15.13	10.89	1.31	15.76	8.18
Total	101.60	100.91	101.12	100.54	101.47	100.95	100.02	100.90	100.24
Cr (ppm)	4238	2243	2797	2916	1857	2968	3016	803.8	2085
Ni	1961	1340	1325	1179	1102	1602	735.9	512.7	1150
Co	141.7	112.4	114.1	53.90	59.71	108.4	64.64	65.48	109.4
V	33.49	54.25	35.90	60.17	32.09	58.79	119.3	47.51	67.62

Table 1. *Cont.*

Sample#	20059	40114	50220	50180	50197	30361	40106	30327	50221
Sc	7.63	12.48	6.16	22.93	9.79	9.57	33.60	10.83	18.28
Li	2.71	9.31	5.27	2.19	6.74	42.85	1.59	22.98	7.13
Cs	0.06	0.17	0.02	0.07	0.05	0.14	0.03	14.46	0.15
Rb	0.43	2.25	1.81	0.78	0.30	5.57	0.92	80.36	7.33
Ba	40.57	70.72	25.36	13.30	37.17	104.2	21.75	630.8	287.7
Sr	10.89	86.98	80.16	6.10	12.30	157.9	21.04	57.36	239.3
Zr	0.77	3.50	1.26	0.76	1.00	2.37	4.50	22.68	4.59
Y	1.25	3.56	1.10	0.92	2.58	3.16	4.02	5.73	2.19
Nb	0.14	0.31	0.01	1.43	1.36	0.62	0.06	5.22	0.17
Ta	0.04	0.03	0.03	1.75	0.06	0.05	0.02	0.76	0.03
Hf	0.02	0.18	0.04	0.04	0.05	0.11	0.24	0.94	0.17
Th	0.14	0.23	0.19	0.30	2.94	0.43	0.18	19.10	0.23
U	0.09	0.13	0.03	0.07	0.09	0.08	0.02	0.09	0.04
La	1.18	1.69	1.09	0.41	14.65	1.27	1.21	48.28	2.01
Ce	2.24	4.77	2.45	0.70	27.24	3.35	2.74	95.34	3.43
Pr	0.25	0.59	0.25	0.10	2.38	0.43	0.32	7.51	0.37
Nd	1.04	2.84	0.99	0.39	8.22	2.27	1.53	23.57	1.46
Sm	0.22	0.68	0.20	0.08	1.10	0.64	0.44	3.10	0.30
Eu	0.05	0.25	0.10	0.04	0.20	0.22	0.17	0.70	0.19
Gd	0.25	0.83	0.27	0.10	1.25	0.80	0.64	3.40	0.41
Tb	0.03	0.13	0.04	0.02	0.13	0.12	0.11	0.34	0.07
Dy	0.22	0.80	0.25	0.16	0.66	0.73	0.78	1.58	0.41
Ho	0.05	0.16	0.05	0.04	0.12	0.14	0.17	0.27	0.10
Er	0.17	0.51	0.17	0.13	0.40	0.43	0.57	0.82	0.31
Tm	0.03	0.07	0.02	0.03	0.05	0.06	0.09	0.10	0.06
Yb	0.24	0.50	0.20	0.22	0.39	0.43	0.2	0.67	0.35
Lu	0.04	0.08	0.03	0.04	0.06	0.07	0.10	0.10	0.06
Ag (ppm)	0.78	0.39	0.18	0.36	0.24	0.28	0.47	0.53	0.38
Cu	36.13	45.71	27.51	37.11	682.53	53.16	39.10	27.48	56.67
Zn	75.97	67.71	83.11	88.04	57.98	72.01	62.42	77.80	78.57
Mo	0.06	0.41	0.18	0.13	0.04	0.08	0.60	0.03	0.24
Pb	0.72	1.22	0.97	0.65	1.27	0.73	1.61	2.08	1.34
Bi	0.08	<0.001	0.11	0.05	0.02	0.03	<0.001	0.07	5.11
Cd	0.02	0.03	0.03	0.03	0.06	0.03	0.05	0.02	0.05
As	0.53	0.32	0.21	0.04	0.30	0.22	0.05	0.60	0.32
Hg	0.59	0.36	4.42	0.08	0.10	0.46	0.40	0.10	0.21
W	8.38	5.22	69.93	1.65	1.07	6.44	7.97	1.36	4.61

Note. Harz—harzburgite; Srp Harz—serpentinized harzburgite; Lherz—lherzolite; Serp—serpentinite.

Table 2. Representative major and trace element compositions of pyroxenites.

Sample#	40090	40171	10030	10035	10038	70884	40129	30342
Rock type	Ol-Web	Ol-Web	Web	Web	Cpxte	Ol-Web	Alt Cpxte	Ol-Web
SiO_2 (wt.%)	51.68	40.29	47.27	49.57	44.90	49.31	44.58	43.84
TiO_2	0.29	0.15	0.37	0.48	0.72	0.34	0.28	0.25
Al_2O_3	3.36	6.29	5.48	4.53	7.85	4.32	18.30	5.44
Fe_2O_3	10.12	11.99	10.21	11.68	11.03	11.81	5.84	7.71
MnO	0.24	0.14	0.17	0.20	0.17	0.19	0.10	0.13
MgO	28.36	28.57	23.42	26.18	20.40	28.26	14.13	29.58
CaO	2.23	4.86	5.46	6.39	12.86	1.63	9.06	6.55

Table 2. *Cont.*

Sample#	**40090**	**40171**	**10030**	**10035**	**10038**	**70884**	**40129**	**30342**
Na_2O	0.25	0.26	0.75	0.51	0.74	0.44	4.10	0.47
K_2O	0.07	0.40	0.10	0.07	0.06	0.15	0.32	0.08
P_2O_5	0.01	0.01	0.01	0.01	0.00	0.03	0.02	0.01
LOI	3.32	7.25	6.81	0.38	1.26	3.43	3.24	5.68
Total	99.94	100.20	100.06	100.00	100.00	99.92	99.96	99.87
Cr (ppm)	2209	1706	2578	2331	1409	2423	564.6	1837
Ni	970.9	3190	936.1	1074	830.4	795.8	284.3	1089
Co	64.42	125.0	66.97	77.0	51.97	74.73	31.67	60.14
V	98.80	42.77	127.6	161.2	216.3	95.97	59.18	72.51
Sc	33.15	12.18	33.30	41.46	54.99	28.57	16.54	19.91
Li	1.94	4.66	13.71	2.52	3.54	7.35	7.05	3.04
Cs	0.34	0.32	0.33	0.08	0.06	0.25	0.43	0.04
Rb	1.77	3.08	1.31	1.02	0.33	2.32	4.14	0.82
Ba	38.26	192.3	246.0	54.01	62.13	52.19	1059	37.24
Sr	18.09	169.6	441.6	73.73	267.6	70.40	1389	113.02
Zr	2.49	3.01	10.49	14.86	25.63	5.70	6.29	4.14
Y	3.95	3.03	6.13	8.44	14.80	3.78	4.85	8.39
Nb	0.40	0.07	0.14	0.19	0.12	0.40	0.14	0.65
Ta	0.03	0.04	0.15	0.09	0.10	0.20	0.06	0.10
Hf	0.16	0.16	0.44	0.65	1.18	0.18	0.32	0.25
Th	0.45	0.13	0.16	0.21	0.07	0.02	0.47	0.28
U	0.08	0.02	0.01	0.03	0.01	0.02	0.05	0.05
La	1.43	1.72	1.94	1.83	2.20	0.77	5.22	1.14
Ce	3.07	3.30	4.35	5.55	8.19	1.75	10.54	4.50
Pr	0.41	0.43	0.64	0.79	1.34	0.22	1.03	0.78
Nd	2.09	2.23	3.27	4.29	8.00	0.91	4.35	4.70
Sm	0.55	0.56	0.97	1.33	2.67	0.28	0.99	1.56
Eu	0.16	0.25	0.39	0.47	0.97	0.12	0.61	0.49
Gd	0.72	0.59	1.26	1.77	3.38	0.41	1.25	1.86
Tb	0.11	0.09	0.20	0.28	0.54	0.08	0.18	0.29
Dy	0.78	0.70	1.28	1.78	3.36	0.52	1.07	1.81
Ho	0.17	0.12	0.26	0.37	0.65	0.14	0.21	0.36
Er	0.52	0.33	079	1.099	1.86	0.42	0.61	1.06
Tm	0.08	0.04	0.11	0.16	0.25	0.08	0.08	0.15
Yb	0.54	0.30	0.75	1.02	1.57	0.48	0.52	0.99
Lu	0.09	0.05	0.12	0.15	0.21	0.09	0.08	0.14
Ag (ppm)	0.57	0.96	0.83	1.55	1.08	0.49	0.44	0.34
Cu	229.41	824.2	208.59	328.23	212.27	51.69	152.14	71.99
Zn	82.57	57.04	56.77	57.90	35.65	80.58	59.25	42.24
Mo	0.29	0.21	0.26	0.72	0.73	0.51	1.20	0.24
Pb	1.03	2.01	2.01	4.27	2.27	0.87	0.44	1.67
Bi	<0.001	17.82	0.13	0.06	0.04	0.06	0.05	<0.001
Cd	0.06	0.09	0.08	0.12	0.15	0.08	0.09	0.09
As	0.10	<0.001	0.05	0.05	0.09	0.21	0.89	0.03
Hg	0.38	0.07	0.35	0.95	0.62	24.77	0.72	0.20
W	7.69	1.89	5.67	14.62	9.94	14.49	15.76	4.02

Note. Ol-Web—olivine websterite; Web—websterite; Cpxte—clinopyroxenite; Alt Cpxte—altered clinopyroxenite.

Table 3. Representative major and trace element compositions of gabbroic and ultramafic metasomatic rocks.

Sample#	**60568**	**60570**	**60585**	**10041**	**10039**	**30243**	**30299**	**30334**
Rock type	Gabbro	Gabbro	Gabbro	Gabbro	Metas	Metas	Metas	Metas

Table 3. *Cont.*

Sample#	60568	60570	60585	10041	10039	30243	30299	30334
SiO_2 (wt.%)	49.31	48.90	50.06	51.00	46.71	38.74	42.58	29.67
TiO_2	0.27	0.23	0.22	0.09	0.32	0.92	4.59	0.08
Al_2O_3	20.75	21.85	21.82	24.89	16.22	10.94	11.52	2.16
Fe_2O_3	4.96	4.84	4.91	2.50	6.84	8.09	11.64	12.52
MnO	0.10	0.09	0.09	0.04	0.10	0.16	0.07	0.34
MgO	8.50	8.49	7.97	6.56	14.56	24.47	15.56	28.98
CaO	10.80	10.44	9.67	8.09	8.84	2.77	2.35	7.32
Na_2O	3.58	3.58	3.30	4.24	2.33	0.95	2.23	0.29
K_2O	0.84	0.47	0.35	0.24	0.17	0.69	3.41	0.12
P_2O_5	0.00	0.01	0.01	0.00	0.01	1.21	0.07	0.01
LOI	0.80	1.04	1.49	2.11	3.96	11.57	6.31	20.67
Total	99.91	99.93	99.88	99.93	100.08	100.53	100.16	102.15
Cr (ppm)	328.4	279.0	169.8	135.6	255.9	120.9	167.0	3656
Ni	103.2	83.43	85.92	93.78	287.9	479.8	275.9	1942
Co	21.77	20.51	20.03	15.53	42.57	51.54	66.21	132.8
V	53.02	54.80	50.15	5.58	105.81	43.13	343.3	54.98
Sc	15.20	17.03	16.60	1.23	28.03	5.27	31.21	5.51
Li	ND	ND	ND	3.09	4.54	49.54	18.15	2.80
Cs	0.29	0.41	0.08	0.08	0.07	0.99	2.46	0.01
Rb	7.05	6.05	1.06	1.38	0.70	26.37	80.46	0.85
Ba	409.3	441.0	104.96	494.1	249.7	1228	7769	293.3
Sr	1004	894.6	812.2	1435	1044	225.6	197.2	1313
Zr	4.43	5.86	3.02	1.27	7.26	8.57	11.28	0.18
Y	3.55	3.76	3.54	0.51	5.57	42.06	33.61	3.73
Nb	0.22	0.25	0.08	0.05	0.19	8.78	2.83	0.03
Ta	0.20	0.16	0.08	0.06	0.11	0.37	0.27	0.01
Hf	0.16	0.22	0.11	0.04	0.33	0.42	0.96	0.01
Th	0.07	0.33	0.19	0.07	0.53	74.53	0.10	0.11
U	0.05	0.07	0.02	0.02	0.02	1.25	0.87	0.09
La	2.00	2.91	2.31	1.18	5.44	505.74	6.09	2.25
Ce	3.98	5.32	4.26	3.08	11.16	978.22	21.15	5.94
Pr	0.50	0.58	0.53	0.29	1.15	83.05	3.20	0.69
Nd	2.066	2.35	2.19	1.16	4.89	272.81	17.99	3.13
Sm	0.49	0.58	0.57	0.19	1.13	32.00	5.89	0.72
Eu	0.40	0.47	0.43	0.39	0.58	5.89	12.59	0.24
Gd	0.56	0.68	0.55	0.20	1.41	35.08	7.44	0.87
Tb	0.10	0.10	0.10	0.02	0.20	2.89	1.17	0.12
Dy	0.59	0.63	0.61	0.12	1.23	11.61	7.35	0.76
Ho	0.13	0.15	0.14	0.02	0.24	1.77	1.46	0.16
Er	0.32	0.39	0.31	0.06	0.70	5.32	4.07	0.51
Tm	0.05	0.06	0.05	0.01	0.09	0.49	0.55	0.07
Yb	0.33	0.32	0.28	0.06	0.60	2.91	3.47	0.54
Lu	0.06	0.06	0.06	0.01	0.08	0.38	0.50	0.09
Ag (ppm)	0.45	0.13	0.46	1.02	0.42	0.60	0.31	0.37
Cu	42.96	34.81	38.44	167.17	124.56	37.16	65.89	243.06
Zn	60.52	86.25	19.51	16.78	40.55	83.99	350.88	61.34
Mo	0.50	0.51	0.47	1.65	0.59	0.05	0.40	0.18
Pb	5.70	4.93	2.73	3.38	2.15	7.54	4.71	2.35
Bi	0.03	0.01	0.04	<0.001	<0.001	0.09	0.03	0.09
Cd	0.12	0.06	0.05	0.04	0.06	0.04	0.02	0.09
As	0.47	0.74	0.48	3.44	7.10	2.85	0.55	1.25
Hg	ND	ND	ND	1.11	0.41	0.09	0.72	4.91
W	11.93	14.39	17.73	22.82	7.03	1.37	14.58	74.75

Note. Metas—metasomatic rocks, ND—not detected.

Table 4. Representative major and trace element compositions of later-stage dikes and veins.

Sample#	**20078 ***	**30359**	**50219 ***	**20062 ***	**20061 ***	**30306 ***	**50218**
Rock type	Bas And	Bas And	Bas And	Gab-Di	Gab-Di	Andesite	Rhyolite
SiO_2 (wt.%)	54.32	54.55	54.56	55.86	57.18	58.72	80.92
TiO_2	0.03	0.36	0.12	0.41	0.09	0.22	0.04
Al_2O_3	13.59	16.29	17.62	17.40	18.56	16.81	6.71
Fe_2O_3	0.66	2.43	1.70	1.29	1.70	0.10	2.05
MnO	0.02	0.04	0.05	0.03	0.04	0.00	0.04
MgO	2.31	5.03	5.22	9.89	7.57	3.06	4.18
CaO	8.36	5.87	3.48	0.88	0.53	2.26	1.18
Na_2O	15.88	6.28	13.22	10.70	11.94	14.27	3.02
K_2O	3.48	4.33	0.10	0.43	0.17	2.02	0.27
P_2O_5	0.00	0.31	0.08	0.18	0.05	0.07	0.01
LOI	1.53	4.65	4.32	3.21	2.53	2.34	1.71
Total	100.08	100.14	100.47	100.28	100.35	99.87	100.13
Cr (ppm)	89.21	107.1	145.4	105.2	107.6	113.6	293.1
Ni	55.12	75.57	62.26	81.39	64.96	33.96	54.74
Co	7.60	12.00	8.51	9.08	9.78	16.71	18.07
V	3.42	16.36	5.08	8.51	28.97	8.07	12.05
Sc	1.04	1.92	3.69	1.46	3.44	1.41	5.89
Li	0.46	2.44	1.24	1.46	1.94	4.39	0.97
Cs	0.02	0.14	0.02	0.03	0.07	0.72	0.10
Rb	16.36	30.71	0.51	2.64	1.57	33.25	9.12
Ba	1523	5876	47.05	297.2	145.6	3242	57.24
Sr	215.1	894.8	484.9	357.0	303.0	2714	197.3
Zr	1.05	2.46	2.56	3.22	1.97	5.90	0.8
Y	0.61	12.18	15.35	13.09	4.47	5.56	2.77
Nb	0.25	3.83	5.18	8.38	1.38	4.42	1.49
Ta	0.04	0.13	0.24	0.33	0.11	0.24	0.05
Hf	0.03	0.18	0.18	0.19	0.08	0.22	0.08
Th	0.23	30.39	20.54	22.98	8.24	8.20	0.26
U	0.10	0.33	1.36	0.32	0.11	0.57	0.19
La	2.04	240.1	129.2	250.5	145.6	58.15	1.27
Ce	3.54	443.9	222.3	452.6	172.9	95.35	2.30
Pr	0.30	35.75	22.14	35.81	93.31	7.45	0.27
Nd	1.01	112.7	75.70	111.7	40.03	25.54	1.12
Sm	0.19	11.94	10.09	12.49	3.98	3.40	0.30
Eu	0.60	2.26	1.64	3.27	0.90	1.60	0.12
Gd	0.21	13.17	7.89	13.93	4.52	3.63	0.43
Tb	0.02	1.02	0.76	1.12	0.34	0.30	0.07
Dy	0.13	3.77	4.13	3.99	1.23	1.42	0.51
Ho	0.02	0.54	0.59	0.57	0.18	0.24	0.11
Er	0.07	1.70	1.57	1.69	0.64	0.74	0.38
Tm	0.01	0.14	0.16	0.14	0.07	0.08	0.07
Yb	0.06	0.81	1.15	0.83	0.54	0.49	0.56
Lu	0.01	0.11	0.17	0.10	0.08	0.07	0.10
Ag (ppm)	0.48	0.43	0.80	0.41	0.35	2.95	0.49
Cu	14.92	21.94	19.86	23.27	10.26	38.71	23.02
Zn	52.86	212.02	10.36	15.64	16.78	145.9	22.20
Mo	0.26	0.85	0.53	0.28	0.57	0.74	2.17
Pb	21.96	20.62	3.17	3.79	3.39	14.13	1.87
Bi	<0.001	<0.001	0.01	<0.001	0.01	0.09	0.08
Cd	0.03	0.04	0.02	0.04	0.04	0.05	0.02
As	0.37	1.32	1.43	0.93	0.29	0.25	0.10
Hg	0.88	0.52	0.47	0.76	0.43	1.08	2.70

Table 4. *Cont.*

Sample#	20078 *	30359	50219 *	20062 *	20061 *	30306 *	50218
W	17.04	11.87	9.65	15.84	8.63	28.77	57.03
Sr/Y	325.6	73.5	31.6	27.3	67.8	488.2	71.2
La/Yb	34.0	296.4	112.4	301.8	175.5	118.7	2.27

Note. *—Partially albitized. Bas And—basaltic andesite; Gab-Di—gabbro-diorite.

4.1. Petrology and Geochemistry of Magmatic and Metasomatic Rocks

4.1.1. Magmatic Rocks

Magmatic rocks in the Ildeus complex include ultramafic rocks ranging from dunite, plagioclase-bearing dunite, harzburgite and lherzolite to olivine websterite, websterite, wehrlite and clinopyroxenite along with petrographically diverse gabbroic rocks (norite, gabbro-norite, gabbro-anorthosite). Ultramafic rocks form the central core of the Ildeus intrusion and are typically rimmed by marginal gabbro-norite (e.g., hole ILN-001 in Figure 1C). Norite and gabbro-anorthosite frequently form thick (up to 50 m) horizons within the ultramafic sequence (e.g., hole ILN-006 in Figure 1C), resulting in a large-scale zoning somewhat similar to the subduction-related Ural-Alaskan dunite-pyroxenite-gabbro complexes (cf., Figure 2 in [88], also [89]). Both dunite/peridotite and websterite/wehrlite units are commonly impregnated by clinopyroxenitic dikes, dikelets and veins. Later-stage clinopyroxenites are, in turn, cross-cut by veins (typically under 5 m, on average 1–2 m thick) and veinlets (1 to 10–30 cm thick) composed of felsic sub-volcanic rocks.

The least metasomatized ultramafic rocks exhibit typical cumulate textures composed primarily of olivine and orthopyroxene with intercumulus plagioclase, amphibole, clinopyroxene and minor biotite (Figure 4). Accessory minerals such as Fe-Mg-Cr-Al spinel, Ti-V- and Cr-magnetite, ilmenite, rutile, zircon, baddeleyite and apatite are commonly observed as inclusions in both cumulus and intercumulus minerals (Figure 5). Mineral abbreviations in all figures and tables follow the nomenclature of [90]. Dunites in the Ildeus complex are typical olivine-rich ortho-, meso- and adcumulates (Figure 4A,B) with plagioclase and amphibole as principal intercumulus phases (Figure 4C,D). Accessory intercumulus minerals include euhedral (primary magmatic) magnetite and cerussite (Figure 5B). Cumulate olivine frequently contains Cr-Mg-Al spinel and Mg-orthopyroxene inclusions, while rims of larger zoned olivine grains are occasionally "peppered" with microinclusions of Ti-V-bearing magnetite and clinopyroxene. Lherzolitic varieties are characterized by a hypidiomorphic to poikilitic texture composed of olivine, orthopyroxene and oxide inclusions in earlier-generation clinopy-roxenes and olivines. Rare wehrlites (forming lenses and horizons up to 10 m thick) display equigranular to weakly porphyritic textures composed of large diopside crystals typically carrying microinclusions of native metals, metal alloys, barite, Fe-Ti oxides and apatite [69,70]. Olivine-rich cumulates also contain disseminated magmatic pentlandite (Figure 4A), chalcopyrite (Figure 4B) and pyrrhotite along with secondary Ni-bearing pyrite, galena, sphalerite, heazlewoodite and digenite [69].

Ol-poor parts of the Ildeus ultramafic sequence are dominated by olivine websterite, websterite and clinopyroxenite (Figure 1C) with meso- and adcumulate textures (Figure 4E). Intercumulus phases in olivine websterites are olivine and orthopyroxene of the later generations as well as amphibole, while in olivine-free websterite and clinopyroxenite, intercumulus is dominated by clinopyroxene and orthopyroxene with minor plagioclase and biotite. Ortho- and clinopyroxenites typically have a granular texture with orthopyroxene or clinopyroxene as the principal, and plagioclase, biotite, Fe-Ti-oxides, apatite and zircon as the minor and accessory mineral phases [69].

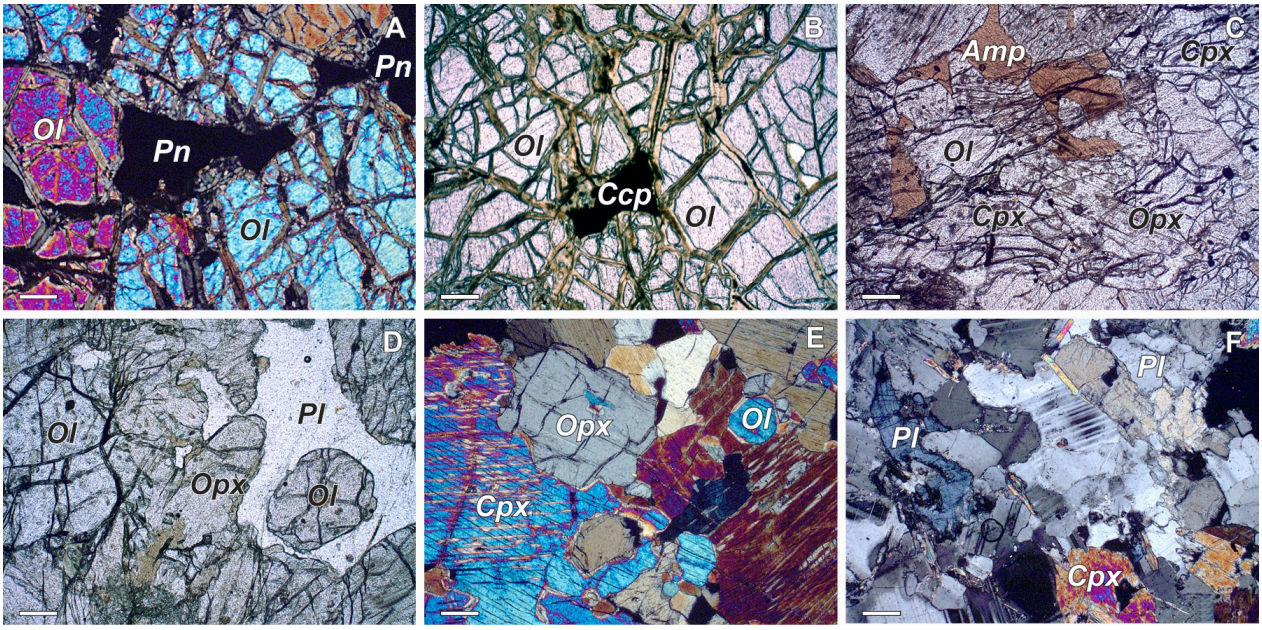

Figure 4. Petrographic features of magmatic rocks from the Ildeus magmatic rocks. (**A**,**B**) Olivine-rich ultramafic cumulates (dunites) with pentlandite (**A**); cross-polarized light) and chalcopyrite ((**B**); plane-polarized light) mineralization. (**C**,**D**) Olivine-pyroxene ultramafic cumulates (lherzolites) with intercumulus amphibole ((**C**); plane-polarized light) and plagioclase ((**D**); plane-polarized light). (**E**) Websterite with equigranular texture (cross-polarized light). (**F**) Gabbro-anorthosite with hypidiomorphic texture (cross-polarized light). Scale bar in all photos is 20 microns. Ol—olivine, Opx—orthopyroxene, Cpx—clinopyroxene, Amp—amphibole, Pl—plagioclase, Pn—pentlandite, Ccp—chalcopyrite.

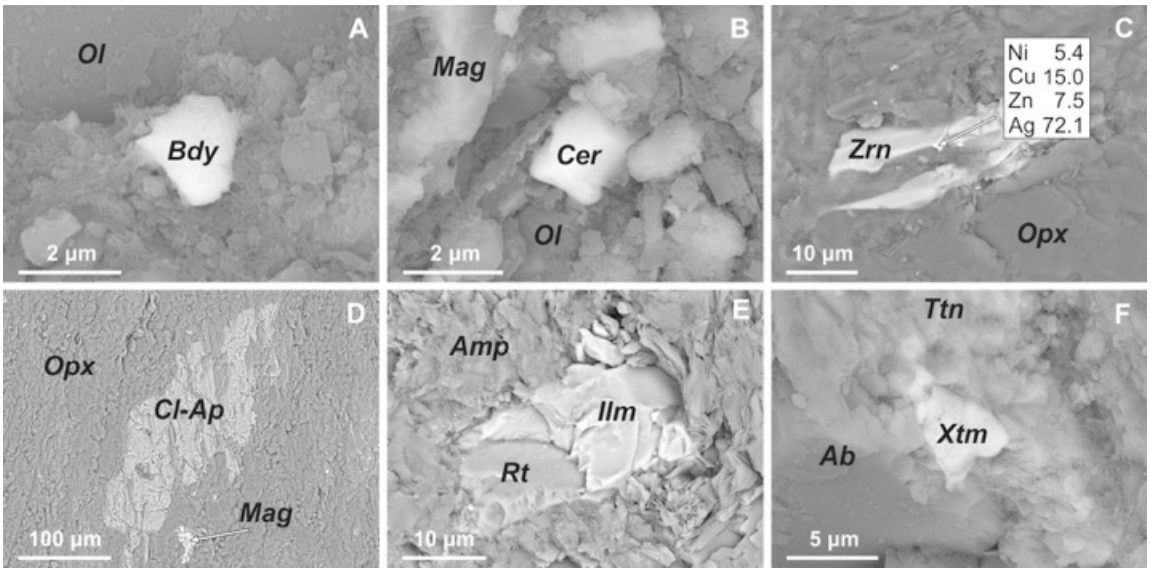

Figure 5. Back-scattered electron (BSE) images of accessory minerals in plutonic rocks from the Ildeus mafic–ultramafic complex. (**A**) Baddeleyite inclusion in cumulate olivine. (**B**) Interstitial euhedral cerussite in association with intercumulus magnetite and olivine. (**C**) Zircon in cumulate orthopyroxene. (**D**) Cl-apatite and magnetite inclusions in orthopyroxene. (**E**) Composite ilmenite-rutile inclusion in late-magmatic amphibole. (**F**). Xenotime and titanite inclusions in metasomatic albite. Ol—olivine, Opx—orthopyroxene, Amp—amphibole, Ab—albite, Bdy—baddeleyite, Mag—magnetite, Cer—cerussite, Zrn—zircon, Cl-Ap—Cl-bearing apatite, Ilm—ilmenite, Rt—rutile, Xtm—xenotime.

Gabbroic rocks appear to be petrographically diverse. Gabbro-anorthosites form thick (first tens of meters), locally almost purely anorthositic layers characterized by a coarse- to medium-grained hypidiomorphic, occasionally poikilitic, texture (Figure 4F) composed of Ca-rich and Ca-Na-plagioclase with minor ortho- and clinopyroxene, biotite and amphibole. Gabbro-norites and norites display hypidiomorphic/granular to poikilitic textures with variable amounts of orthopyroxene, clinopyroxene and plagioclase, minor olivine (in olivine gabbro and norite), amphibole and biotite, and accessory Ti-magnetite, ilmenite, titanite, rutile, zircon, Cl-apatite and (La-Ce-Nd)- and Y-bearing silicates and phosphates (allanite, monazite and xenotime).

Silicate mineral compositions in Ildeus cumulates show systematic variations from ultramafic to gabbroic lithologies. Olivines in dunites and peridotites have Mg/(Mg + Fe) in the range of ~88–90, while olivine compositions in websterites, wehrlites and pyroxenites are distinctly more ferrous (Fo 84–89) [69]. A decrease in olivine Fo-content is accompanied by a gradual decrease in Ni and increase in MnO content in olivine and the onset of plagioclase and amphibole crystallization in the intercumulus matrix of dunites and peridotites [69]. Minor components (CaO, Al_2O_3, TiO_2 and, in most cases, Cr_2O_3) in olivines from the Ildeus mafic–ultramafic complex are present only in almost negligible amounts (0.00–0.01 wt.%; Table 1 in [69]). Orthopyroxenes in peridotites are bronzites and enstatites with relatively high Al and Ti concentrations, while clinopyroxenes are mostly diopsides with elevated Al_2O_3 and Na_2O contents [69]. Late-magmatic (both in the intercumulus and partial rimming and replacing of pyroxenes) amphibole exhibits variable Al_2O_3 contents (4–12 wt.%). Intercumulus plagioclase in dunite and peridotite is bytownite and labradorite, while plagioclase compositions in gabbro and gabbro-anorthosite correspond to labradorite, andesine and oligoclase [69].

Major element variations in dunites, peridotites, websterites, pyroxenites and gabbros from the Ildeus complex suggest their derivation from a common picritic or Mg-rich basaltic magma through polybaric fractionation of olivine, orthopyroxene, clinopyroxene, plagioclase and amphibole [69,70,83]. Ildeus plutonic rocks are generally MgO-enriched and follow a calc-alkaline (low Fe/Mg) differentiation trend [91] on the AFM diagram and, with the exception of gabbro-anorthosites and intermediate to felsic veins, dikes and dikelets (compositions with high total alkali contents in Figure 6A), plot into the field [92] of arc-related cumulate plutonic rocks (Figure 6A). The trace element distribution in mafic–ultramafic rocks from the Ildeus intrusion normalized to the primitive mantle [93] show their general enrichment in large-ion lithophile elements (LILEs), such as Ba, Sr and Rb and light rare-earth elements (La and Ce) coupled with the pronounced depletion in high-field-strength elements (HFSEs), such as Nb, Ta, Zr and Hf, a feature characteristic of subduction-related magmatic rocks [94,95].

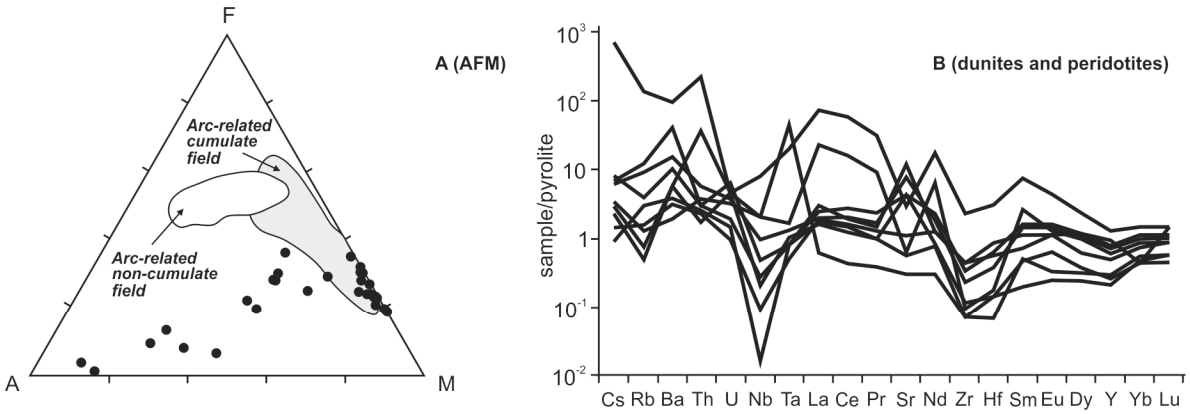

Figure 6. *Cont.*

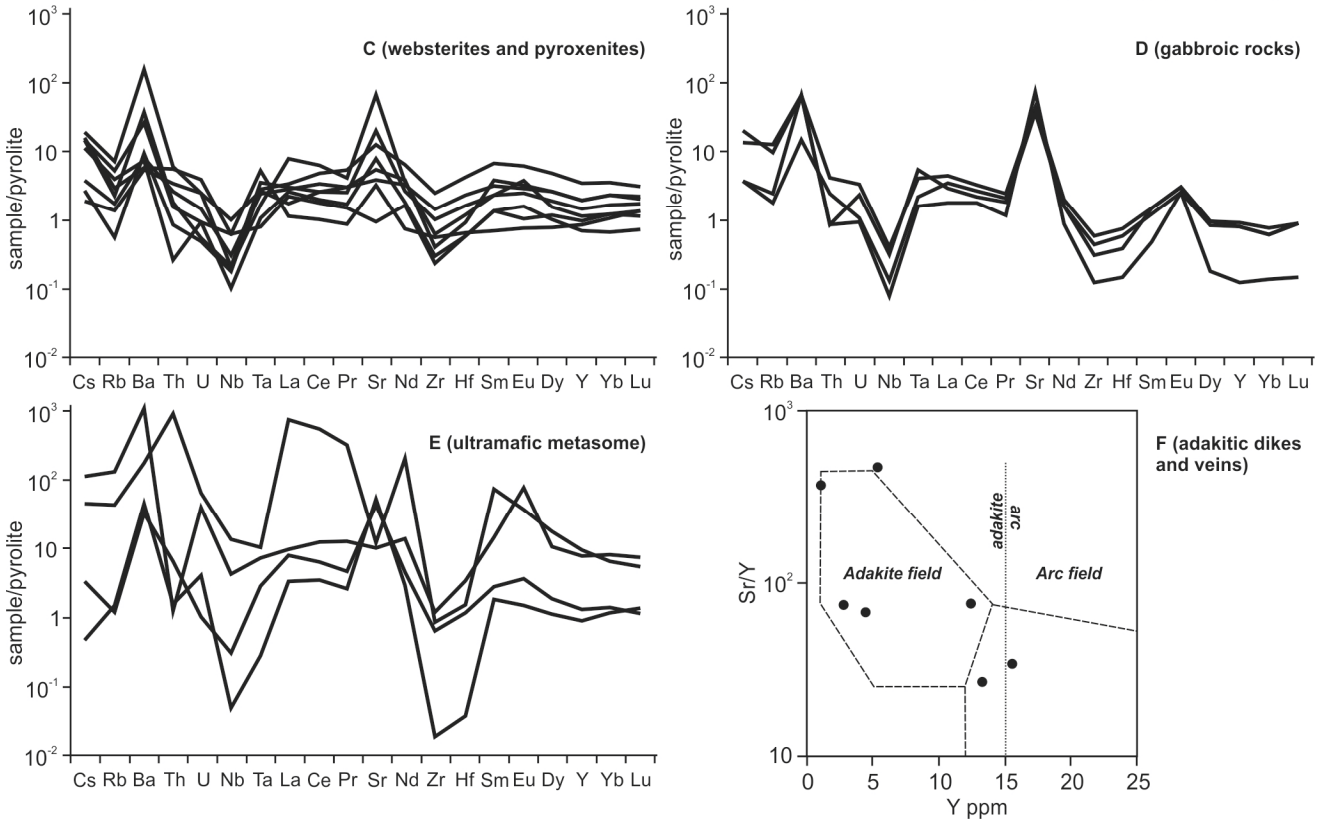

Figure 6. Major and trace element variations in plutonic and metasomatic rocks from the Ildeus mafic–ultramafic complex. (**A**) A (Na_2O + K_2O)—F (total Fe)—M (MgO) discrimination diagram. Arc-related cumulate and non-cumulate compositional fields are from [92]. (**B**–**E**) Primitive mantle-normalized incompatible element patterns for magmatic and metasomatic rocks from the Ildeus complex. Normalizing values from [93]. (**F**) Sr/Y versus Y (ppm) discrimination diagram for felsic veins and dikes. Compositional fields for adakites and arc rocks and adakite/normal arc discrimination line are from [64].

4.1.2. Metasomatic Rocks

Metasomatic rocks in the Ildeus magmatic–hydrothermal system can be sub-divided into two groups on the basis of their principal mineral assemblages: (1) ultramafic metasomes composed mainly of talc, chlorite and serpentine with variable amounts of carbonate and (2 quartz-rich metasomes with minor amounts of albite, orthoclase, adularia, biotite, chlorite, calcite, sericite and muscovite. Textures of metasomatic rocks range from relic porphyroclastic (Figure 7C,E,F) to glomeroblastic and crystalloblastic with some relics of igneous mineralogy still recognizable in thin sections (Figure 7B,D). Dunite and harzburgite protoliths within ultramafic metasomes are frequently completely serpentinized with typical mesh and hourglass textures (Figure 7A). Carbonates frequently form ultrathin (0.05–0.5 mm) discordant veinlets cross-cutting the serpentine-talc (±chlorite) matrix (Figure 7A).

Ultramafic metasomes in the Ildeus complex display substantial scatter in the concentrations of many chemical components (Table 3) including such refractory metals as Cr (120–3655 ppm) and Ni (93–1942 ppm), large-ion lithophile elements Rb (0.7–80 ppm), Sr (97–1435 ppm) and Ba (293–7769 ppm), as well as high-field strength elements Nb (0.05–8.78 ppm) and Th (0.07–74.53 ppm). Metasomatic rocks also exhibit substantial variations in SiO_2 (29.67–51.00 wt.%), TiO_2 (0.08–4.59 wt.%), Al_2O_3 (2.16 -24.89 wt.%), MgO (6.56–28.98 wt.%), K_2O (0.12–3.41 wt.%) and P_2O_5 (0.01–1.21 wt.%) (Table 3). The observed major and trace element variations in ultramafic metasomes within the Ildeus complex appear to be linked to changes in modal contents of principal metasomatic mineral phases,

such as talc, serpentine, chlorite, potassic feldspar, albite, Ti-magnetite, ilmenite, rutile and apatite [69,83]. Exceptionally high Rb (80.46 ppm) and Ba (7769 ppm) concentrations in some samples (e.g., sample 30299 in Table 3) appear to be related to the presence of modal mica (both biotite and muscovite), Ba-rich (up to 3 wt.% based on SEM-EDS determinations) potassic feldspar and barite in these metasomatic rocks from the Ildeus complex.

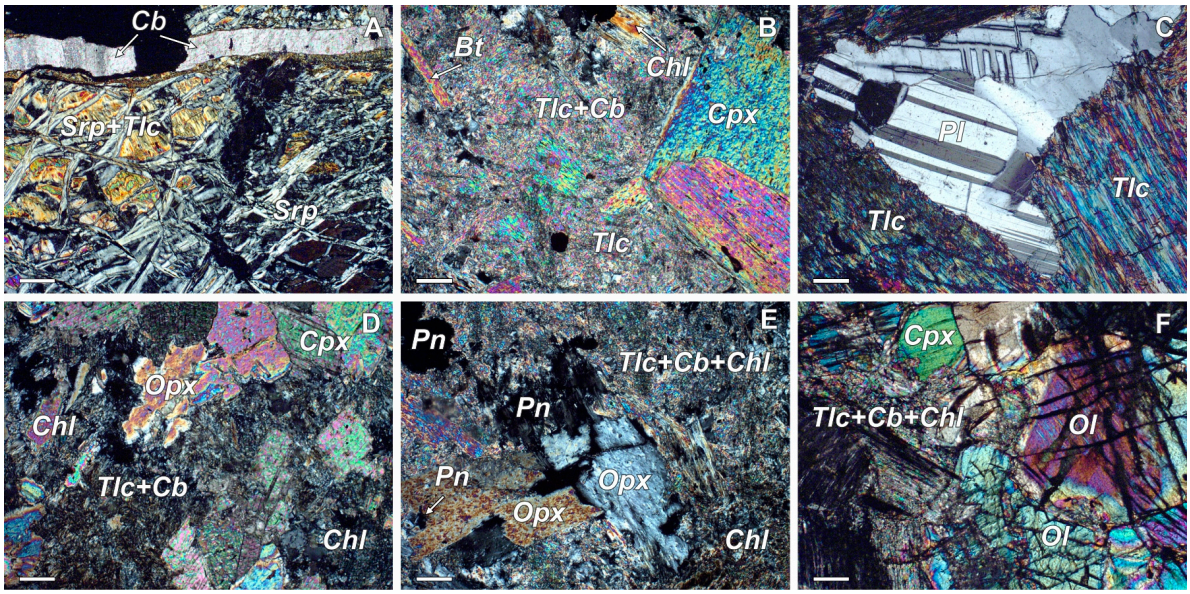

Figure 7. Petrography of ultramafic metasomes in the Ildeus plutonic complex. (**A**) Crystalloblastic, predominantly serpentine-talc metasome with later-stage carbonate veinlets. (**B**) Glomeroblastic talc-chlorite-carbonate metasome with relic clinopyroxene and biotite crystals. (**C**) Porphyroclastic talc-dominated metasome with relic intercumulus plagioclase. (**D**) Glomeroblastic talc-carbonate-chlorite metasome with relic hypidiomorphic clino- and orthopyroxene crystals. (**E**) Porphyroclastic talc-carbonate-chlorite metasome with relic orthopyroxene and intergranular pentlandite mineralization. (**F**) Olivine-clinopyroxene adcumulate with some cumulate iron-magnesian silicates replaced with fine-grained talc-carbonate-chlorite aggregate. All photos are taken in cross-polarized light, scale bar is 20 microns. Mineral abbreviations: Ol—olivine, Cpx—clinopyroxene, Opx—orthopyroxene, Bt—biotite, Pl—plagioclase, Srp—serpentine, Tlc—talc, Cb—carbonate, Chl—chlorite, Pn—pentlandite.

4.2. Metal Assemblages in Plutonic and Metasomatic Rocks

Plutonic and metasomatic rocks from the Ildeus mafic–ultramafic complex are characterized by diverse associations of native metals, metal alloys, sulfides, sulfates, sulfasalts and halides. Some examples of these metal assemblages were previously described in [69,70]. Below, we present new extended data set for metal assemblages from the Ildeus mafic–ultramafic complex.

4.2.1. Native Metals and Alloys

Siderophile metals in peridotites and pyroxenites from the Ildeus complex are represented by euhedral to subhedral inclusions of platinum with minor iron and copper in cumulate-textured clinopyroxene (Figure 8A), orthopyroxene (Figure 8B) and olivine (Figure 8C). The euhedral grain of Fe-Pt alloy in Figure 8B is almost completely enclosed in magmatic orthopyroxene, suggesting magmatic origin for the platinum alloy.

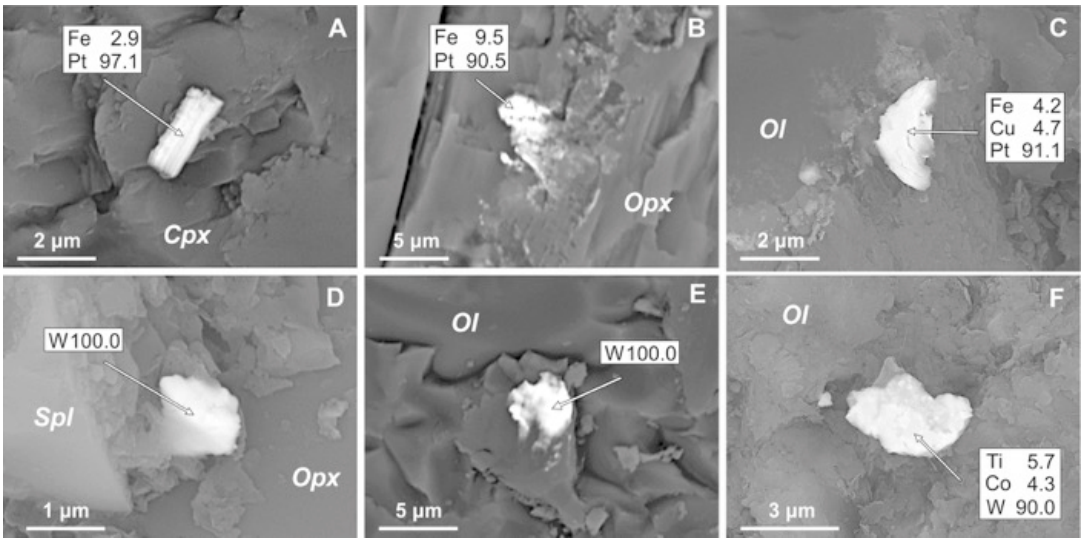

Figure 8. BSE images of siderophile metals and alloys in primary magmatic minerals. (**A**) Euhedral Fe-bearing platinum crystal included in clinopyroxene. (**B**) Fe-bearing platinum inclusion in orthopyroxene. (**C**) Fe-Cu-Pt alloy included in olivine. (**D**) Native tungsten inclusion in orthopyroxene. (**E**) Native tungsten inclusion in olivine. (**F**) Co-Ti-W inclusion in olivine. Ol—olivine, Opx—orthopyroxene, Cpx—clinopyroxene, Spl—spinel. Insets here and in Figures 9–18 display tabulated element contents in mas.%, and arrows depict exact positions of the SEM-EDS analyses.

Cumulate-textured magmatic minerals, such as olivine, carry inclusions of native tungsten (Figure 8E) and Co-Ti-W alloy (Figure 8F). A subhedral particle of native tungsten was also observed in the intersticial space between the Cr-Fe-Mg-Al spinel and orthopyroxene crystals in the least altered harzburgitic cumulate (Figure 8F).

Another siderophile metal common to the Ildeus ultramafic system is gold, which occurs as a native element (Figure 9) and as an alloy with copper and silver (Figure 10). Native gold forms lumpy microinclusions (typically about 1–3 microns in size) in cumulate-textured clinopyroxene (in association with magnetite; Figure 9A) and orthopyroxene (Figure 9B), as well as serpentine replacing some larger grains of cumulate olivine (Figure 9C). Gold–silver alloys have been observed in cumulate olivine (Figure 9D) and orthopyroxene partially replaced with chlorite (Figure 9E), as well as in secondary chlorite in ultramafic metasome (Figure 9F). Some Ag-Au alloys in partially (Figure 9E) or completely (Figure 9F) altered ultramafic rocks display a vuggy appearance possibly due to the deposition from and interaction with later-stage hydrothermal fluids.

Gold also commonly forms ternary Cu-Ag-Au alloys observed as microinclusions in cumulate olivine (Figure 10A) and orthopyroxene (Figure 10C). Cu-Ag-Au alloy included in magmatic olivine contains minor chlorine and is texturally closely associated with non-stoichiometric silver chloride (Figure 10A). Another Cu-Ag-Au particle was observed in the fracture within the larger clinopyroxene crystal and can be possibly of the later-stage magmatic or metasomatic origin. Copper–silver–gold alloys also frequently occur in secondary silicate minerals in both partially altered plutonic rocks and ultramafic metasomes as inclusions in serpentine (Figure 10D), albite (Figure 10E) and Ba-rich orthoclase (Figure 10F).

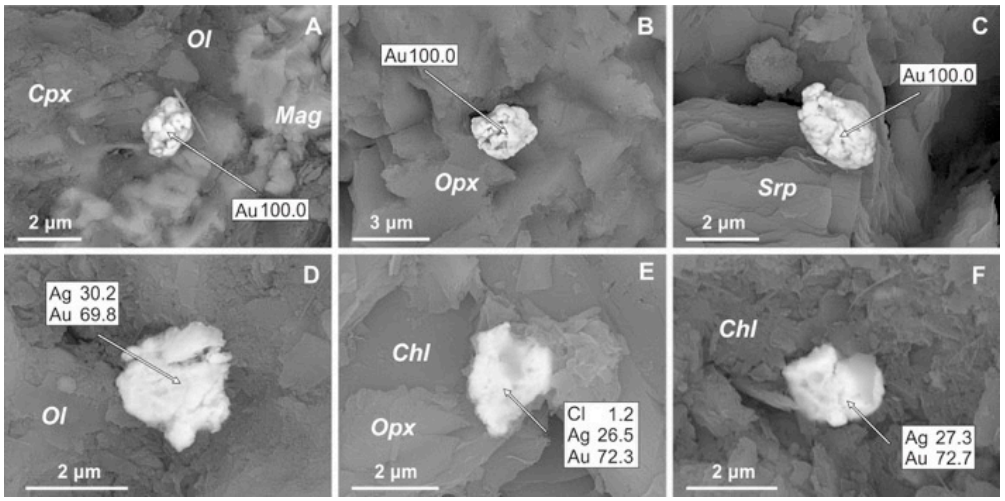

Figure 9. BSE images of native gold and silver–gold alloys. (**A**) Interstitial gold inclusion associated with olivine, clinopyroxene and magnetite. (**B**) Gold inclusion in orthopyroxene. (**C**) Gold inclusion in serpentine. (**D**–**F**) Silver–gold alloy inclusions in (**D**) olivine, (**E**) partially chloritized orthopyroxene (with minor chlorine) and (**F**) chlorite. Ol—olivine, Opx—orthopyroxene, Srp—serpentine, Chl—chlorite, Mag—magnetite.

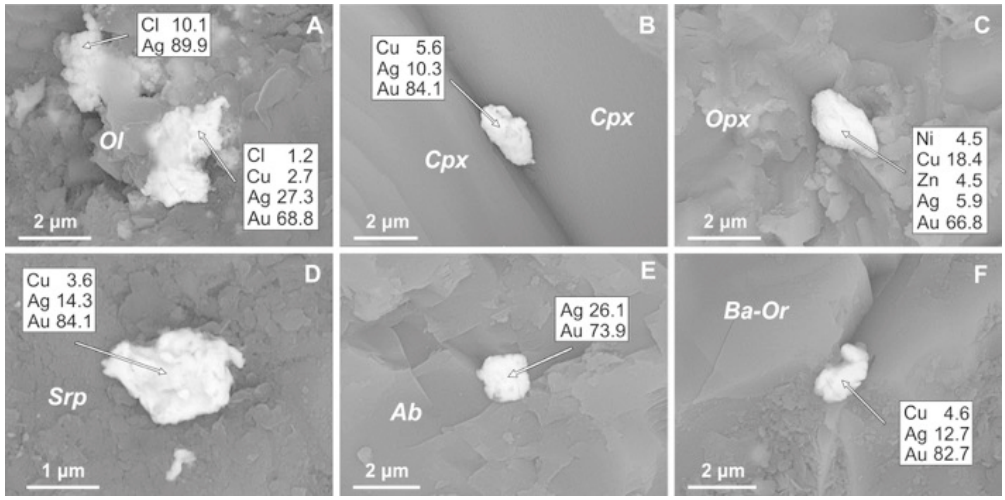

Figure 10. BSE images of copper–silver–gold alloys. (**A**) Cu-Ag-Au (with minor Cl) inclusion in olivine in association with silver chloride. (**B**) Cu-Ag-Au inclusion inside a fracture within larger clinopyroxene grain. (**C**) Cu-Ag-Au inclusion in orthopyroxene.. (**D**) Cu-Ag-Au inclusion in serpentine. (**E**) Ag-Au inclusion in albite. (**F**) Interstitial Cu-Ag-Au inclusion between two grains of Ba-rich orthoclase. Ol—olivine, Cpx—clinopyroxene, Opx—orthopyroxene, Srp—serpentine, Ab—albite, Ba-Or—Ba-rich orthoclase.

Magmatic (cumulate), late-magmatic (interstitial) and metasomatic silicate minerals also frequently contain cupriferous silver particles, which is the most frequent metal alloy phase in the Ildeus mafic–ultramafic complex by modal abundance (Figure 11).

Cu-Ag alloy is observed intergrown with intercumulus olivine along the contact with the larger cumulus olivine grain (Figure 11A). Inclusions of cupriferous silver in cumulate orthopyroxene (Figure 11B) and intercumulus plagioclase (Figure 11C) as well as late-stage magmatic or metasomatic biotite (Figure 11D) are also quite common. A single grain of Cu-Ag alloy in association with magnetite and ilmenite is included in hydrothermal Fe-rich chlorite (Figure 11E). Secondary-textured potassic feldspar occasionally contains minute particles of anhedral cupriferous silver (Figure 11F).

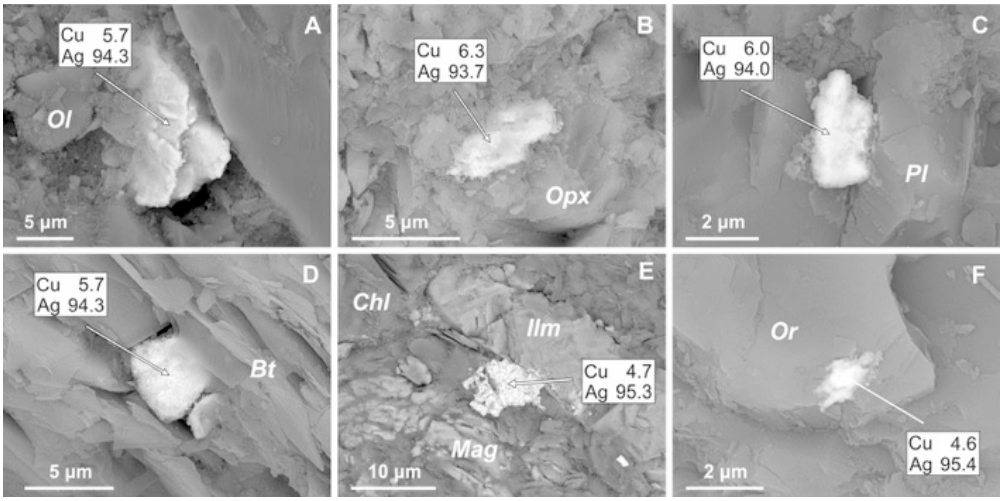

Figure 11. BSE images of Cu-Ag alloy inclusions in (**A**) olivine (Ol), (**B**) orthopyroxene (Opx), (**C**) plagioclase (Pl), (**D**) biotite (Bt), (**E**) chlorite (Chl) in association with magnetite (Mag) and ilmenite (Ilm), and (**F**) orthoclase (Or).

Refractory metals in Ildeus plutonic rocks are associated with binary and ternary alloys and minerals of chalcophile elements (Figure 12). Olivine and orthopyroxene in ultramafic cumulates contain nickel–copper (Figure 12A), copper–zinc (Figure 12B,C), copper–zinc–silver (Figure 12D) and lead–tin (with minor chlorine) inclusions (Figure 12E). We have also previously reported the occurrence of natural bronze and brass along with Cu-Ag-Sn-Zn and Zn-Cu-Ag alloys in Ildeus ultramafic rocks [69]. Secondary orthoclase and chlorite also contain minute cassiterite inclusions of (Figure 12F; [69]).

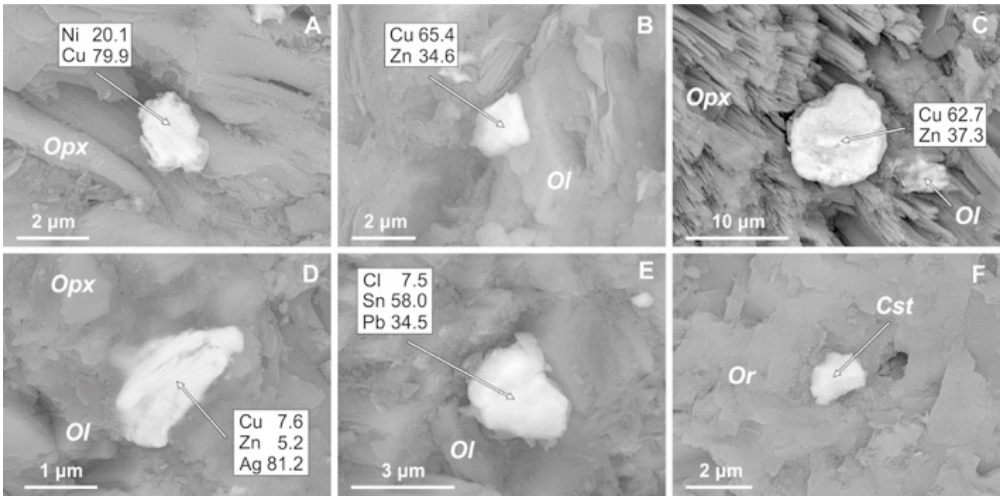

Figure 12. BSE images of alloys and minerals of chalcophile metals. (**A**) Inclusion of Ni-Cu alloy in orthopyroxene. (**B**,**C**) Inclusions of Zn-Cu alloy (natural brass) in olivine (**B**) and orthopyroxene in association with minute olivine inclusion (**C**). (**D**) Zinc–copper–silver alloy intergrown with orthopyroxene and olivine. (**E**) Chlorine-bearing lead–tin inclusion in olivine. (**F**) Inclusion of cassiterite in orthoclase. Ol—olivine, Opx—orthopyroxene, Or—orthoclase, Cst—cassiterite.

4.2.2. Halides

Halides of chalcophile elements (Cu, Ag, Bi, Te) occur as microinclusions in rock-forming silicate minerals in the Ildeus mafic–ultramafic complex (Figure 13).

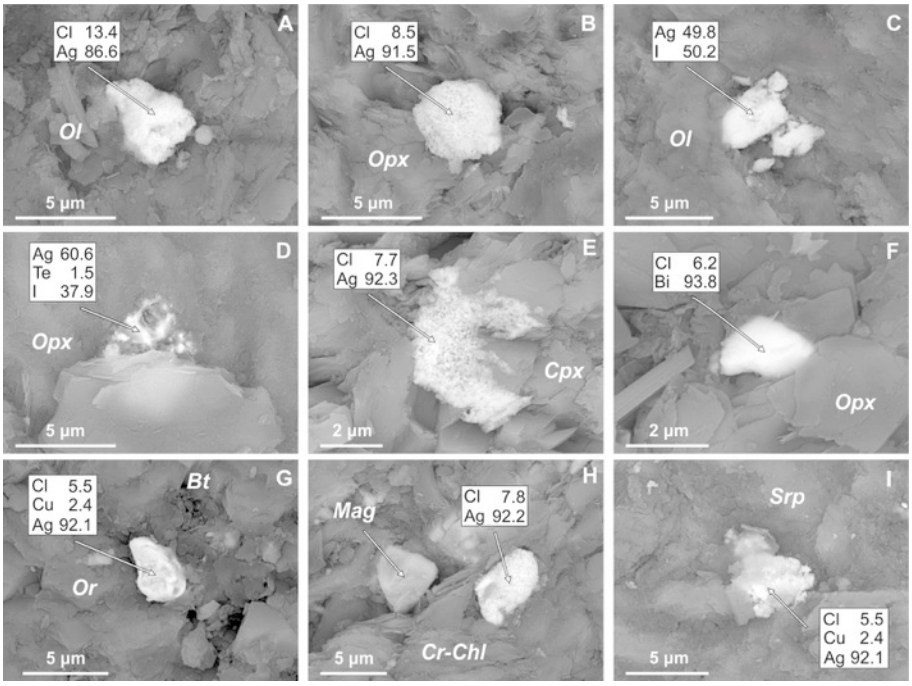

Figure 13. BSE images of halides of chalcophile elements. (**A**,**B**) Inclusions of silver chloride in (**A**) olivine and (**B**) orthopyroxene. (**C**,**D**) Inclusions of silver iodide in (**C**) olivine and (**D**) orthopyroxene (with minor Te). (**E**) Inclusions of silver chloride in clinopyroxene. (**F**) Inclusion of bismuth chloride in orthopyroxene. (**G**) Interstitial subhedral grain of copper–silver chloride at the contact between orthoclase and biotite. (**H**) Inclusions of silver chloride in association with magnetite in Cr-rich chlorite. (**I**) Inclusion of copper–silver chloride in serpentine. Ol—olivine, Opx—orthopyroxene, Cpx—clinopyroxene, Bt—biotite, Or—orthoclase, Mag—magnetite, Cr-Chl—Cr-rich chlorite, Srp—serpentine.

Non-stoichiometric silver chloride is included in cumulate olivine (Figure 13A), orthopyroxene (Figure 13B) and clinopyroxene (Figure 13E) of clear magmatic textural origin. Silver iodide (iodargyrite) occurs in the core of the cumulate olivine (Figure 13C) and, with minor Te, in the core-to-rim zone of a cumulate orthopyroxene (Figure 13D). A single inclusion of non-stoichiometric bismuth chloride was found in fine-grained intercumulus orthopyroxene (Figure 13F). Non-stoichiometric copper–chlorine–silver compound was observed intergrown with secondary potassic feldspar and biotite (Figure 13G) and serpentine (Figure 13I). Another non-stoichiometric silver chloride particle occurs together with magnetite in hydrothermal chrome-rich chlorite grain (Figure 13H).

4.2.3. Sulfides, Sulfates, Sulfosalts

Both cumulate magmatic and secondary hydrothermal silicate minerals are associated with a compositionally wide range of sulfide, sulfate and sulfosalt microinclusions (Figures 14–18). Primary Ni-Co-Cu sulfides in the Ildeus complex include pentlandite, Co-pentlandite, pyrrhotite, chalcopyrite and bornite [69,96]. Co-pentlandite frequently forms cores of composite inclusions rimmed by magnetite in olivine (Figure 14A). Pentlandite occurs as inclusions in cumulate olivine and pyroxene, and intercumulus amphibole (Figure 14B). It also forms discrete interstitial grains between cumulate olivines (Figure 4A) and intercumulus grains in association with interstitial amphibole, calcic plagioclase and biotite [69,96].

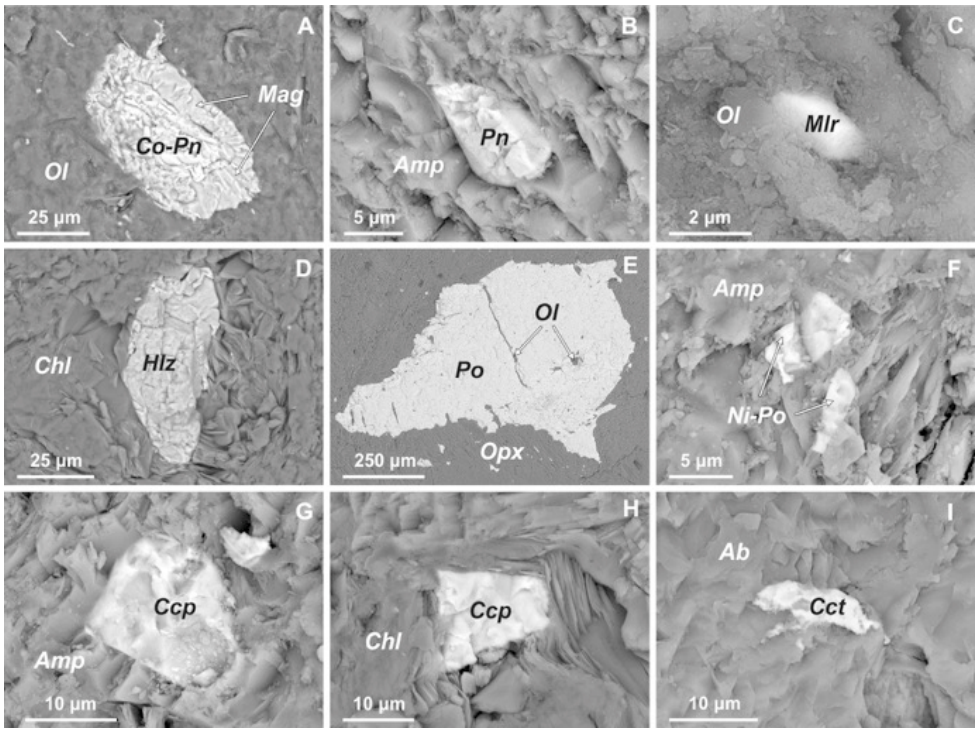

Figure 14. BSE images of Ni-Co-Cu sulfides. (**A**) Zoned Co-pentlandite (core)—magnetite (rim) inclusion in olivine. (**B**) Pentlandite inclusion in amphibole. (**C**) Millerite inclusion in olivine. (**D**) Heazlewoodite inclusion in chlorite. (**E**) Large (1 mm) grain of pyrrhotite with olivine microinclusions enclosed in a cumulate orthopyroxene crystal. (**F**) Inclusion of Ni-bearing pyrrhotite in amphibole. (**G**,**H**) Inclusions of chalcopyrite in amphibole (**G**) and chlorite (**H**). (**I**) Inclusion of chalcocite in albite. Ol—olivine, Opx—orthopyroxene, Amp—amphibole, Chl—chlorite, Ab—albite, Mag—magnetite, Co-Pn—Co-pentlandite, Pn—pentlandite, Mlr—millerite, Hlz—heazlewoodite, Po—pyrrhotite, Ni-Po—Ni-bearing pyrrhotite, Ccp—chalcopyrite, Cct—chalcocite.

Other Ni-sulfides comprise minute inclusions of millerite in cumulate olivine (Figure 14C) and heazlewoodite in hydrothermal chlorite (Figure 14D). Large pyrrhotite grains in cumulate orthopyroxene contain fine inclusions of equigranular olivine, indicating that some Fe-Ni sulfides were part of the early fractionating magmatic assemblage (Figure 14E). Some intercumulus amphiboles contain Ni-bearing (1–3 wt.%) pyrrhotite (Figure 14F). Chalcopyrite (occasionally with bornite [69,83]) is frequently included in interstitial amphibole (Figure 14G) and secondary chlorite (Figure 14H). Another (in addition to digenite [69]) hydrothermal copper sulfide is represented by elongated chalcocite inclusions in secondary albite (Figure 14I).

Galena forms euhedral to subhedral inclusions in hydrothermal rock-forming silicates such as serpentine (Figure 15A) and orthoclase (Figure 15B). Amphibole contains inclusions of lead sulfide with minor Ni and Fe (intergrown with sphalerite; Figure 15D) and Zn, Cu and Fe (Figure 15D). In addition, Cu-bearing galena is observed as anhedral equant inclusions in chlorite (Figure 15E) and orthoclase (Figure 15F).

In addition to galena and sphalerite, both magmatic and metasomatic minerals in the Ildeus complex contain diverse composite sulfides of nickel, iron, copper, zinc and lead (Figure 16). Magmatic olivine in ultramafic cumulate contains elongated tabular grains of Fe-Ni-Zn-sulfide (Figure 16A). Cumulate orthopyroxene contains a minute (~2 μm) inclusion of Cu-Fe-bearing sphalerite (Figure 16B). One lath of interstitial late-magmatic biotite associated with intercumulus orthopyroxene carries several anhedral equant inclusions of composite Ni-Fe-Zn and Co-Ni-Fe-Zn sulfides (Figure 16C). Ba-rich metasomatic orthoclase contains a zoned inclusion composed of Ni-Zn-Fe-Cu sulfide and Fe-Cu-Zn-bearing galena (Figure 16D). Microinclusions of Fe-As-Cu-bearing galena are also present in secondary albite (Figure 16E) and Ba-rich orthoclase (Figure 16F).

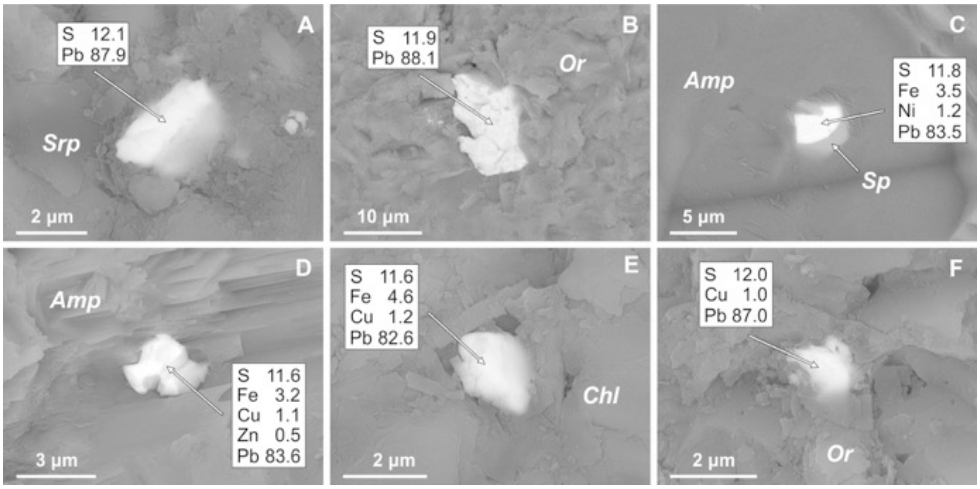

Figure 15. BSE images of galena and composite lead sulfides. (**A**,**B**) Galena inclusions in (**A**) serpentine and (**B**) orthoclase. (**C**) Intergrowth of Ni-Fe-Pb sulfide with sphalerite included in amphibole. (**D**) Inclusion of composite Zn-Cu-Fe-Pb sulfide in amphibole. (**E**) Inclusions of composite Cu-Fe-Pb sulfide in chlorite. (**F**) Inclusion of copper-bearing lead sulfide in orthoclase. Srp—serpentine, Or—orthoclase, Amp—amphibole, Sp—sphalerite, Chl—chlorite.

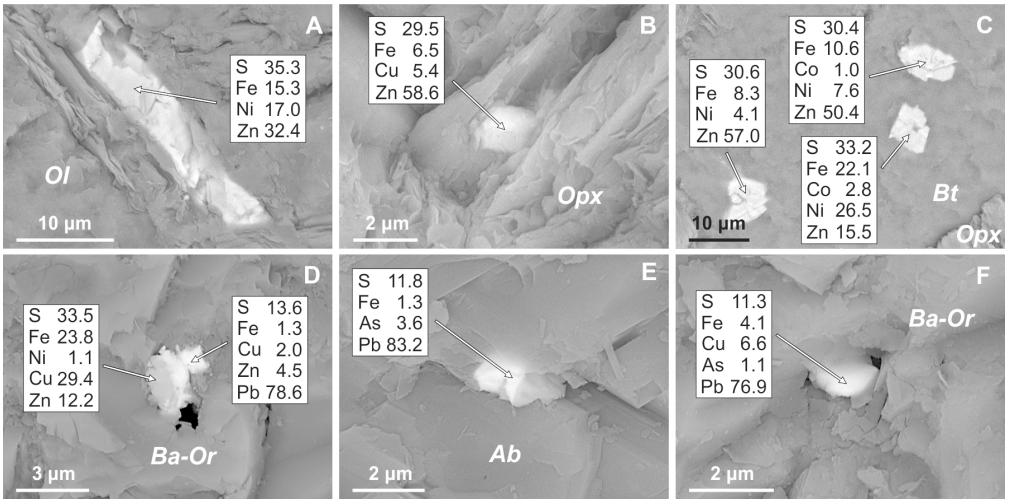

Figure 16. BSE images of composite sulfides of chalcophile and siderophile metals. (**A**) Euhedral inclusion of Ni-Fe-Zn sulfide in olivine. (**B**) Inclusion of Cu-Fe-bearing sphalerite in orthopyroxene. (**C**) Inclusions of Ni-Fe-bearing and Co-Ni-Fe-bearing sphalerite along with composite Co-Zn-Fe-Ni sulfide in biotite in contact with orthopyroxene. (**D**) Inclusions of Ni-Zn-Fe-Cu and Fe-Cu-Zn-Pb composite sulfides in Ba-rich orthoclase. (**E**) Inclusion of Fe-As-bearing galena in albite. (**F**) Inclusion of As-Fe-Cu-Pb-bearing galena in Ba-rich orthoclase. Ol—olivine, Opx—orthopyroxene, Opx—orthopyroxene, Bt—biotite, Ba-Or—Ba-rich orthoclase, Ab—albite.

Copper–silver sulfides are other common sulfides of chalcophile metals observed in both primary- and secondary-textured silicates in the Ildeus plutonic suite (Figure 17).

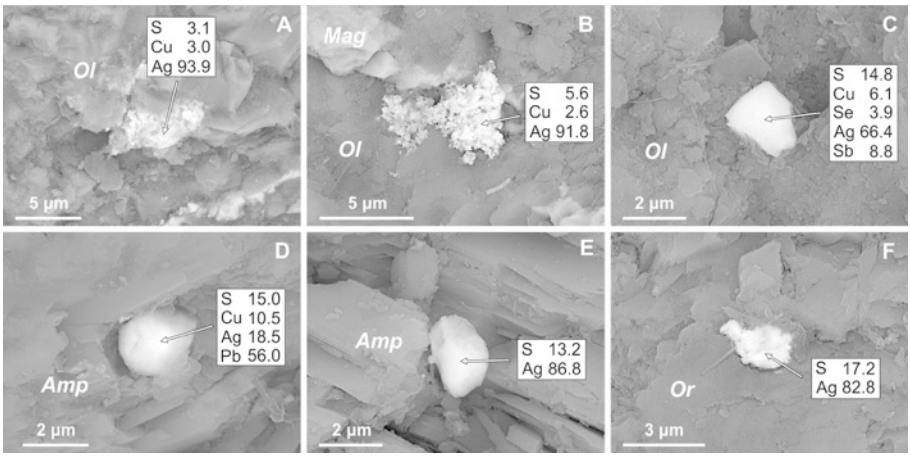

Figure 17. BSE images of silver and copper sulfides and sulfosalts. (**A**,**B**) Inclusions of non-stoichiometric copper–silver sulfide in olivine. (**C**) Inclusion of Cu-Ag-Se-Sb-sulfosalt in olivine. (**D**) Inclusion of Cu-Ag-Pb sulfide in amphibole. (**E**,**F**) Inclusion of silver sulfide in amphibole (**E**) and orthoclase (**F**). Ol—olivine, Amp—amphibole, Mag—magnetite, Or—orthoclase.

Copper-bearing silver sulfide forms distinct botryoidal aggregates included in cumulate olivine (Figure 17A,B). A single cumulate olivine crystal also contains an euhedral inclusion of Cu-Ag-Se-Sb sulfosalt (Figure 17C). Intercumulus amphibole carries equant, almost spherical inclusions (~2 µm in size) of Cu-Ag-Pb sulfide and non-stoichiometric acanthite (Figure 17D,E). A similar acanthite grain is also included in secondary potassic feldspar (Figure 17F).

Sulfides and sulfosalts of siderophile and chalcophile metals are frequently associated with barite in Ildeus plutonic rocks. Euhedral barite forms microinclusions in cumulate olivine (Figure 18A) and orthopyroxene (Figure 18B). In both cases, barite is almost completely enclosed by host magmatic silicates, suggesting a high-temperature origin for at least some early barite grains. Barite occurs as rims on magnetite crystals in intercumulus orthopyroxene (Figure 18C). It is also frequently included in secondary hydrothermal silicates such as serpentine (Figure 18D) and epidote together with feldspar inclusions (Figure 18E), or occurs as an interstitial phase together with pyrite along the contact between plagioclase and Ba-rich potassic feldspar crystals (Figure 18F).

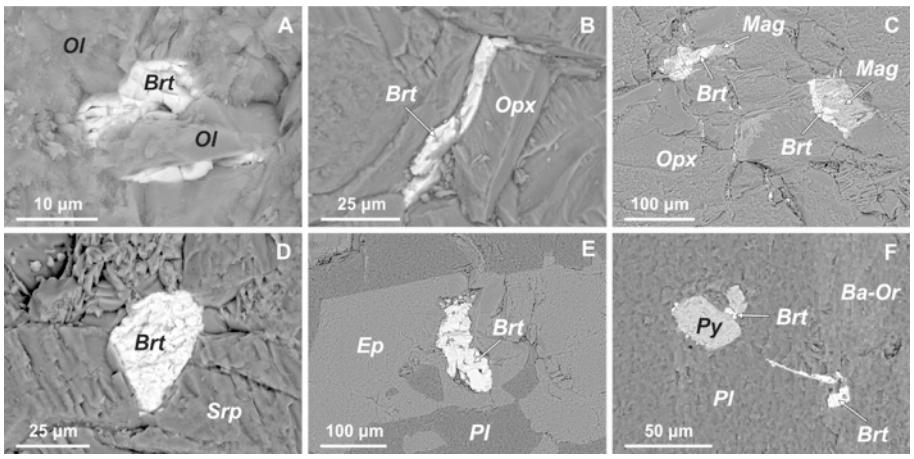

Figure 18. BSE images of barite (Brt) microinclusions. (**A**,**B**) Barite inclusions in olivine (**A**) and orthopyroxene (**B**). (**C**) Zoned barite-magnetite inclusions in orthopyroxene. (**D**) Barite inclusion in orthopyroxene. (**E**) Barite inclusion in epidote in association with plagioclase. (**F**) Barite inclusions in association with pyrite in plagioclase and Ba-rich orthoclase. Ol—olivine, Opx—orthopyroxene, Mag—magnetite, Srp—serpentine, Ep—epidote, Pl—plagioclase, Ba-Or—Ba-rich orthoclase, Py—pyrite.

4.3. Geochemistry of Noble Metals

Platinum-group element (PGE) and Au concentrations and some inter-element ratios in the Ildeus complex are listed in Table 5. All plutonic and metasomatic rocks display wide variations in bulk PGE and Au contents as well as in Pt/Ir, Pd/Ir and Au/Ir ratios.

Table 5. Concentrations of platinum-group elements and gold in representative plutonic and metasomatic rocks from the Ildeus mafic–ultramafic complex.

Ir (ppb)	Ru (ppb)	Rh (ppb)	Pt (ppb)	Pd (ppb)	Au (ppb)	Pt/Ir	Pd/Ir	Au/Ir
Dunite and peridotite								
0.68	0.50	0.43	0.85	1.76	4.87	1.25	2.59	7.16
0.51	1.02	0.48	192.38	1.39	9.57	377.2	2.73	18.8
0.69	0.39	0.36	5.14	1.36	39.31	7.45	1.97	56.9
0.35	0.22	0.19	242.26	73.95	16.50	692.2	211.3	47.1
0.18	0.33	0.45	11.00	12.44	2.40	61.1	69.1	13.3
0.53	1.05	0.30	12.89	3.32	8.47	24.3	6.26	16.0
0.96	1.14	0.30	9.24	0.18	11.49	9.63	0.19	11.9
0.88	1.89	0.64	17.15	0.23	28.74	19.5	0.26	32.7
0.30	1.54	0.59	2.39	1.98	47.37	7.97	6.60	157.9
0.03	0.75	0.14	1.24	3.47	14.03	41.3	115.7	467.7
0.30	1.33	0.80	2.71	8.79	7.20	9.03	29.3	24.0
0.13	1.11	0.61	22.43	10.81	53.43	172.5	83.2	411.0
0.24	0.63	0.71	1.87	14.83	33.33	7.79	61.8	138.9
0.65	0.45	0.48	4.35	6.53	3.92	6.69	10.1	6.03
Websterite and clinopyroxenite								
0.39	0.42	0.42	6.08	3.29	9.72	15.6	8.44	24.9
0.20	0.87	0.89	2.42	1.79	140.85	12.1	8.95	704.3
0.55	0.75	0.30	3.62	1.23	190.40	6.58	2.24	346.2
0.22	0.72	0.21	2.61	0.54	48.49	11.9	2.45	220.4
0.16	0.55	0.31	1.86	7.09	144.80	11.6	44.3	905.0
0.48	0.71	0.27	2.61	2.07	62.18	5.44	4.31	129.5
0.36	0.99	0.49	3.23	4.77	5.17	8.97	13.3	14.4
0.11	1.27	0.39	2.03	3.50	45.21	18.5	31.8	411.0
Gabbro								
0.13	0.40	0.24	2.65	0.08	8.30	20.4	0.64	63.8
0.30	0.52	0.22	2.06	0.42	16.83	6.87	1.40	56.1
0.02	0.66	1.80	27.02	34.24	8.65	1351	1712	432.5
0.05	0.33	0.12	2.56	4.89	9.37	51.2	97.8	187.4
Ultramafic metasome								
0.59	0.53	0.50	18.79	1.33	21.63	31.8	2.25	36.7
1.21	0.84	0.81	14.19	6.94	13.64	11.7	5.74	11.3
0.29	0.48	0.40	8.30	1.73	12.12	28.6	5.97	41.8
0.33	0.66	0.46	3.80	2.98	13.44	11.5	9.03	40.7
0.43	0.45	1.31	17.64	11.09	10.87	41.0	25.8	25.3
1.03	2.34	1.14	192.12	15.68	10.54	186.5	15.2	10.2
1.57	4.00	2.50	43.63	22.44	25.44	27.8	14.3	16.2
0.25	0.63	0.26	4.30	0.69	7.07	17.2	2.76	28.3
0.59	0.66	0.35	2.22	0.24	773.72	3.76	0.41	1311
0.86	0.39	0.24	2.69	3.38	102.53	3.13	3.93	119.2
0.75	1.26	0.68	2.08	4.09	77.27	2.77	5.45	103.0
1.39	3.60	1.28	16.44	10.41	132.57	11.8	7.49	95.4
1.41	10.15	2.36	21.11	7.20	149.60	15.0	5.11	106.1
Adakitic veins and dikelets								
0.24	0.30	0.56	1.25	3.45	48.06	5.21	14.4	200.3
0.94	0.62	0.21	1.05	1.00	32.17	1.12	1.06	34.2
0.39	0.59	0.41	1.10	2.49	75.38	2.82	6.38	193.3
4.26	0.04	1.10	1.10	13.90	6.25	0.26	3.26	1.47
0.46	0.28	0.57	1.90	7.48	9.01	4.13	16.3	19.6

For example, Pt contents in Ildeus rocks range from 0.85 to 242 ppb, Pd—from 0.18 to 74 ppb, and Au—from 2.4 to 773 ppb. Some olivine websterites from the Ildeus complex are extraordinarily enriched in gold and contain up to 596 ppm Au [70]. Concentrations of Pd-group elements (Pd, Pt) in the Ildeus complex with few exceptions substantially exceed Ir-group (Ir and Ru) metal contents (Pt/Ir = 1.25–692; Pd/Ir = 1.97–211). Gold is also typically enriched compared to refractory Ir-group PGEs (Au/Ir = 1.47–468) and also shows variable compositional relationships with the Pd-group metals (Table 5). Adakites display relatively narrow variations in Pd-group PGE contents (Pt = 1.1–1.9 ppb; Pd = 1.0–13.9 ppb) in comparison with mafic and ultramafic rocks, while Au concentrations in adakites range substantially from 6.25 to 75.38 ppb (Table 5).

Variations in chondrite-normalized noble metals in Ildeus plutonic and metasomatic rocks are summarized in Figure 19. Average compositions of the upper continental crust [97], pelagic clay [98], arc basalt [43], island arc mantle [3], primitive mantle [93] along with the compositional field for the Ural-Alaskan-type mafic–ultramafic complexes [99], are shown for comparative purposes. Average compositions of principal lithologies from the Ildeus complex plot into the field of Ural-Alaskan-type mafic–ultramafic complexes and display well-defined Pt- and Au-enriched chondrite-normalized noble metal patterns (Figure 19). Gold enrichments, somewhat similar to the Ildeus rocks, are also observed in arc basalts and mantle wedge peridotites (Figure 19), indicating that this might be a geochemical feature characteristic of subduction zone environments in general [2–4]. Later-stage adakites display PGE-Au patterns almost identical to ultramafic melasomes and gabbro (Figure 19), which may reflect certain broad similarities in the geochemical processes involved in their formation.

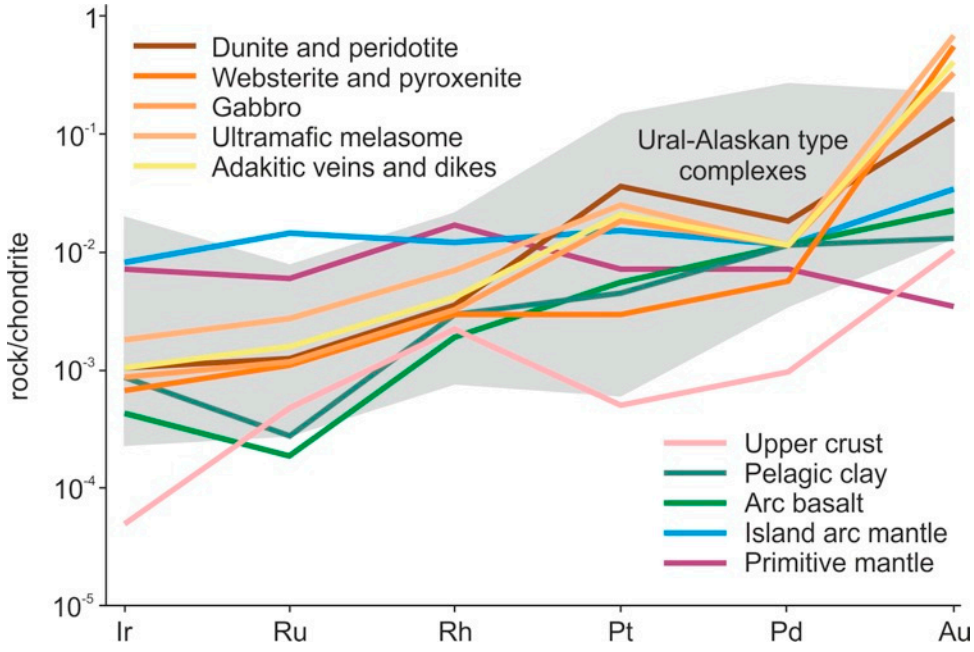

Figure 19. Distribution of PGE and Au in plutonic and metasomatic rocks as well as late-stage adakite veins and dikes compared with the average upper crust [97], pelagic clay [98], Ural-Alaskan-type mafic–ultramafic complexes [99], arc basalt [43], primitive mantle [93] and island-arc mantle [3]. All samples are normalized to chondrite [93].

5. Discussion

5.1. Ildeus Mafic–Ultramafic Complex as a Plutonic Root System of Mesozoic Magmatic Arc

The Ildeus mafic–ultramafic complex was emplaced into the predominantly mafic Precambrian crust (amphibolites, mafic gneisses and two-pyroxene crystalline schists) beneath the Mesozoic (Triassic) mature magmatic arc or active continental margin [69,70,81–83]. This Mesozoic magmatic arc records a northward subduction of the Mongol–Okhotsk

oceanic basin under the southern edge of the Precambrian Aldan shield [81,82,100]. Arc-type magmatism persisted over the course of at least 100 Ma in the Triassic and Early Jurassic [69] before the collision between the Amur superterrane (North Amur craton) and Siberian craton and the final closure of the Mongol–Okhotsk ocean in the Middle to Late Jurassic [80,81]. The Jurassic collision event was followed by an Early Cretaceous extension marked by adakite and high-Nb lamprophyre dikes in the Stanovoy suture zone [69] and prolific alkaline magmatism in the South Aldan region [101–103]. The Middle to Late Jurassic collision and localized Early Cretaceous post-collision rifting resulted in the remobilization of some Triassic–Early Jurassic magmatic complexes and their emplacement in the uppermost crust followed by the re-working of mafic and ultramafic rocks by crustal hydrothermal fluids [69].

An Ildeus plutonic suite was produced through crystal fractionation of olivine, clinopyroxene, orthopyroxene and Cr-Al-spinel in a lower- to mid-crustal igneous plumbing system beneath the mature Mesozoic magmatic arc [69,70]. The mineralogy and textures of Ildeus mafic–ultramafic rocks are similar to typical arc cumulates [92,104,105] as well as experimental products of magmatic differentiation of primitive convergent zone magmas [106,107]. The late-stage crystallization of plagioclase and Al-rich amphibole in the Ildeus plutonic sequence is also characteristic of the polybaric fractionation of water-saturated mafic magmas fractionated in sub-arc crustal conditions [92,108]. Pressure estimates for Ildeus plutonic rocks based on various Al-in-hornblende barometers correspond to approximate sub-arc depths of 15–25 km (~4–6 kbars), which is consistent with general geologic observations as well as structural data [69].

Major oxide variations in plutonic rocks from the Ildeus complex indicate that they generally follow island arc tholeiite and calc-alkaline differentiation trends (Figure 6A). The presence of well-defined HFSE (Nb, Ta, Hf, Zr) depletions coupled with variable but generally high concentrations of LILE (Cs, Rb, Ba, Sr) and LREE in ultramafic and mafic plutonic rocks as well as ultramafic metasomes (Figure 6) suggest their derivation from HFSE-depleted hydrous mafic magma in the mature arc geodynamic context [69,70,83]. Geologic and structural data coupled with petrologic reconstructions support the interpretation of the Ildeus complex as a plutonic root system of the Mesozoic Stanovoy arc comparable in many aspects to subduction-related mafic–ultramafic intrusions in Phanerozoic orogenic belts [89,96,104].

5.2. Magmatic to Hydrothermal Evolution of Metals in the Ildeus Complex

Metal assemblages hosted in high- and low-temperature rock-forming minerals in plutonic and metasomatic rocks appear to reflect three principal stages of crustal evolution of the Ildeus mafic–ultramafic complex.

Olivine and pyroxene in ultramafic cumulates frequently contain (Table 6) microinclusions of high-temperature refractory metals (W, Pt, Au) and their alloys (Fe-W, Ti-Co-W, F-Pt, Ni-Rh-Pt, Pd-Pt, etc.), suggesting early magmatic origin for siderophile metals in the Ildeus complex [69,70]. High-temperature siderophile metals are frequently associated with Ni-Co-Cu-Fe sulfides (pentlandite, Co-pentlandite, pyrrhotite, Ni-pyrrhotite, bornite, chalcopyrite), which occur either as interstitial phases or inclu-sions in Mg-rich olivine and Mg-pyroxenes (Figure 14A,C,E). Magmatic silicates also contain microinclusions of Cu-Ag-Au, Ni-Cu-Zn-Ag-Au and Sn-Zn-Cu-Ag alloys and native Zn, Bi and Pb [69,70,96], suggesting either the enrichment of parental Ildeus melt in these elements or the existence of favorable crustal conditions, which facilitated the precipitation of siderophile and chalcophile metals. Phase equilibria in systems Ti-Co-W and Cu-Ag-Au indicate the formation of some alloys included in olivine and pyroxenes in the temperature range of 800–1200 °C, which is generally comparable with the temperature range for the fractional crystallization of a typical calc-alkaline igneous suite [106,107]. The droplet-like appearance of some Ni-Co-Cu sulfides also suggests that liquid immiscibility may have played a certain role during early stages of the Ildeus magma evolution [69,70,96]. Early-magmatic-stage metals, alloys and sulfides are also associated with barite, silver halides (non-stoichiometric chlo-

rargyrite and iodargyrite; Figure 13A–E), Pb-Sn chloride and Cl-apatite (Table 6), indicating the involvement of Cl-S-rich fluids [69,96].

Table 6. Metal and mineral assemblages in magmatic and metasomatic rocks from the Ildeus mafic-ultramafic complex.

Stages of Evolution	Metal and Mineral Assemblages			
	Native Metals	**Alloys**	**Sulfides, Sulfosalts, Halides, Sulfates, Tellurides**	**Associated Minerals**
Early magmatic stage	W, Pt, Zn, Bi, Pb, Au	Fe-W, Ti-Co-W, Fe-Pt, Cu-Pt, Ni-Rh-Pt, Pd-Pt, Ni-Cu, Cu-Zn, Cu-Ag, Sn-Zn-Cu, Zn-Cu-Ag, Cu-Ag, Cu-Ag-Au, Cu-Ag-Au-Zn-Ni	Pn, Co-Pn, Po, Mlr, Ccp, Bn, Cu-Ag-S, Fe-Ni-Co-Zn-S, Ag_2S, Brt, Pb-Sn-Cl, AgCl, AgI	Ol, Mg-Opx [(1)], Cpx, Mg-Fe-Cr-Al Spl, Mag, Ilm, Ttn, Rt, Cl-Ap
Late magmatic stage	Au	Cu-Ag, Pb-Sb, Ni-Ag-Zn-Cu-Au, Zn-Cu-Au, Cu-Sn	Pn, Po, Ni-Po, Bn, Mlr, Co-Ni-Sp, Co-Ni-Zn-S, Ag_2S, Cu-Ag-Pb-S, Ni-Gn, Sp, Brt	Fe-Opx [(2)], Amp [(3)], Bt, Pl, Mag, Ilm, Ttn, Ap, Bdy, Zrn, Qz, Cer, Aln, Dol
Metasomatic-hydrothermal stage	Ag, Zn, Ni, Au	Cu-Ag-Au, Ag-Au, Cu-Ag, Cu-Zn	Pn, Ccp, Cct, Dg, Hzl, Py, Brt, Cst, Cu-Ag-S, Ag_2S, Gn, Cu-Gn, Sb-Pb-Cl, Ag-Cl-S, Cu-Ag-Cl, AgCl, Bi-Cl, Cu-Sb-Ag-Se-S, Cu-Pb-Fe-As-S, Pb-As-S, Cu-Pb-As-S, Ag_2S, Fe-Cu-Zn-Pb-S, Ni-Zn-Fe-Cu-S, Cu-Ag-Pb-Se-Te	Tlc, Chl, Srp, Tr, Cb, Ep, Ab, Or, Ba-Or, Qz, Mag, Rt, Ttn, Aln, Mnz, Xtm

This table includes data from [69,70]. [(1)] Mg-rich orthopyroxene (enstatite/bronzite). [(2)] Fe-rich orthopyroxene (hypersthene). [(3)] Al-rich (5–12 wt.% Al_2O_3) pargasitic hornblende [69]. Mineral abbreviations: Ab—albite, Aln—allanite, Amp—amphibole, Ap—apatite, Cl-Ap—Cl-rich apatite, Ba-Or—Ba-rich orthoclase, Bdy—baddeleyite, Bn—bornite, Bt—biotite, Cb—carbonates, Ccp—chalcopyrite, Cct—chalcocite, Cer—cerussite, Cpx—clinopyroxene, Cst—cassiterite, Dg—digenite, Dol—dolomite, Ep—epidote, Gn—galena, Cu-Gn—Cu-bearing galena, Ni-Gn—Ni-bearing galena, Hzl—heazlewoodite, Ilm—ilmenite, Mag—magnetite, Mlr—millerite, Mnz—monazite, Ol—olivine, Opx—orthopyroxene, Or—orthoclase, Pl—plagioclase, Pn—pentlandite, Co-Pn—Co-rich pentlandite, Po—pyrrhotite, Ni-Po—Ni-bearing pyrrhotite, Py—pyrite, Rt—rutile, Sp—sphalerite, Co-Ni-Sp—Co- and Ni-bearing sphalerite, Spl—spinel, Tr—tremolite, Ttn—titanite, Xtm—xenotime, Zrn—zircon.

Late-stage magmatic evolution of the Ildeus complex was dominated by the crystallization of intercumulus plagioclase and amphibole along with Fe-rich pyroxenes followed by partial replacement of early-stage Mg-rich silicates by amphibole, biotite and Cr-rich chlorite [69]. Later-stage amphibole, Ca-Na plagioclase and Fe-rich orthopyroxene contain microinclusions of native gold, cupriferous silver, Ni-Ag-Zn-Cu-Au, Cu-Sn and Pb-Sb alloys, along with pentlandite, millerite, Ni-pyrrhotite, chalcopyrite, bornite, sphalerite (with minor Co and Ni), galena (with minor Ni and Cu), Cu-Ag-sulfide and barite (Table 6). Textural evidence suggests that some Ni-Co-Cu sulfides could represent relic magmatic phases preserved during the late-stage replacement of high-temperature silicates by metasomatic amphibole, biotite and chlorite (Figure 14B,F–H). The presence of minor Co and Ni in sphalerite and Ni and Cu in galena (Figures 15C–F and 16A–D) probably reflects the perseverance of refractory metals in late- to post-magmatic metasomatic reactions [109,110]. Besides galena and sphalerite, late-stage magmatic metal assemblages include Ag and Cu-Ag-Pb sulfides and sulfosalts (Figure 17), indicating a high activity of volatile chalcophile elements (Pb, Zn and Ag) during the final stages of evolution of the Ildeus magmatic system. This is consistent with high concentrations of these metals in melt inclusions and volcanic gases in modern volcanic arcs [111–113].

Metal assemblages generated during early and late magmatic differentiation in the Ildeus arc root plutonic complex were further upgraded during prolonged (millions of years [69,83]) and complicated metasomatic processes linked to the late subduction and collision processes at the Stanovoy convergent plate margin [69,70,83,96]. Metasomatic reactions involving the replacement of magmatic olivine + pyroxene + amphibole with serpentine, chlorite, talc, tremolite and carbonate resulted in the formation of new metal associations as well as partial preservation of relic native Zn, Ni, Ag [69,70,96] and Au (Figure 9C) along with Sn-Pb (Figure 12E), Cu-Ag (Figure 11E,F), Cu-Ag-Au (Figure 10D,F) and Ag-Au (Figure 10E) alloys (Table 6). The abundance of Au-bearing alloys in metasomatic rocks is consistent with the strong bulk gold enrichment observed in some ultramafic metasome samples (Figure 19). Primary Ni-Co-Cu sulfides were upgraded and supplemented with secondary digenite and heazlewoodite (Figure 14D), chalcocite (Figure 14I), galena (Figure 15A,B), acanthite (Figure 17E,F), composite Cu-Pb-Fe (Figure 15E) and Cu-Zn-Pb-Fe (Figure 16D) sulfides, as well as Pb-Fe-Cu sulfosalts (Figure 16E,F; Table 6). Secondary native metals, alloys, sulfides and sulfosalts are associated with non-stoichiometric Cu-Ag-chlorides (Figure 13G–I), barite (Figure 18D–F) and pyrite (Figure 18F). The association of Cu-Ag-halides (common minerals in volcanic fumaroles [114]), Cu-Pb-arsenides and Cu-Ag-Pb tellurides [69] with barite and pyrite in both ultramafic and quartz-rich metasomes in the Ildeus complex suggest the involvement of oxidized H-S-Cl fluid typical of some subduction and post-subduction epithermal environments [115]. These fluid-induced metasomatic reactions most probably took place during final emplacement of the Ildeus intrusion under shallow upper crustal conditions beneath the collision-related Stanovoy suture [69,70,83,96].

Our mineralogical and micro-metallogenic observations presented in this section and summarized in Table 6 suggest that refractory metal assemblages, such as PGE alloys, W and its alloys, CuAg-Au alloys and primary Ni-Co-Cu sulfides, crystallized from hydrous mafic melts sourced in the metal-rich mantle wedge above the Mesozoic Stanovoy subduction zone. The existence of metal-rich mantle wedge sources in arcs has been previously proposed on the basis of geochemical and mineralogical data [2–4,8,68]. The occurrence of halide inclusions in olivine, orthopyroxene and clinopyroxene in association with Cl-apatite suggests the formation of an early magmatic native metal-alloy–sulfide assemblage in the Ildeus complex under H-S-Cl-fluid-saturated conditions at the base of the Mesozoic Stanovoy arc [69,96]. Early magmatic metal assemblage (native Ag, Au, Zn, Ni metals [69,96], Cu-Ag-Au and Cu-Zn alloys) was further upgraded during late-magmatic and metasomatic stages through the addition of secondary Ni-Cu (heazlewoodite, digenite, chalcocite), Cu-Ag, Ag (acanthite), Fe-Cu-Zn-Pb-S and Ni-Zn-Fe-Cu sulfides as well as various Cu-Pb-Sb-Ag sulfosalts (Table 6). The association of secondary non-stoichiometric Cu-Ag, Ag and Bi chlorides (Figure 13G–I) and Ag-Cl-S with abundant barite inclusions in orthoclase, chlorite, albite and serpentine indicates the high activity of oxidized (sulfate S) H-S-Cl fluids during the final stages of Ildeus system evolution in the upper crust.

5.3. Geochemical Constraints on Fluid-Induced Metal Transport at Arc Plutonic Roots

The abundance and distribution of W, Mo, Cu and their isotopes in igneous rocks have been previously successfully used to reconstruct fluid regimes and redox conditions facilitating metal cycling in the crust–mantle system at convergent plate boundaries [116–123]. Figure 20 summarizes the distribution of siderophile (W, Mo) and chalcophile (Cu, Zn, As, Ag, Cd, Hg, Pb, Bi) elements in plutonic and metasomatic rocks from the Ildeus complex along with the later-stage felsic dikes. Average compositions of oceanic (abyssal) and supra-subduction peridotite, arc websterite and gabbro, pelagic clay, arc volcanic rocks (Nicaragua, Cascades, Kuriles, Kamchatka and Japan) as well basaltic glass from Hawaii and composite hydrothermal fluid are shown for comparison. Plutonic rocks from the Ildeus complex are characterized by fractionated siderophile and chalcophile element patterns normalized to the average upper continental crust (Figure 20A–E). Ultramafic–mafic rocks, ultramafic metasomes and later-stage felsic dikes share prominent As-Cd-Pb

depletions and Ag-W-Hg enrichments, although some distinctions exist between various magmatic and metasomatic lithologies. Dunites/peridotites and websterites/pyroxenites are enriched in Bi in comparison with the upper continental crust, while the latter display more prominent enrichments in Ag and W (Figure 20B). Ultramafic cumulates are quite compositionally different (prominent Cu-Ag-W-Hg-Bi enrichments and As-Pb depletions) from abyssal peridotites and similar to the supra-subduction ultramafic rocks (Figure 20A). Ildeus websterites and gabbros are enriched in all elements from Ag to Bi with respect to websterite and gabbro from Kurile and the Papua New Guinea arc basement (Figure 20B,C; [124]). UCC-normalized patterns for ultramafic metasome from the Ildeus complex resemble quite remarkably the reconstructed hydrothermal fluid composition (Figure 20D). Finally, later-stage adakitic dikes display negative As and positive Ag anomalies (Figure 20E) similar to modern arc lavas (Figure 20F) at the same time, drastically differing from them in behavior of such elements as W and Pb. In general, ultramafic rocks from the Ildeus complex display low Zn, As, Mo, Cd and Pb contents and are enriched in Ag, W and Hg with respect to the average upper continental crust. Gabbroic rocks have Ni, Co, Cu, Zn and Cd concentrations similar to the continental crust and are slightly depleted in As and Pb and enriched in Ag and W. Felsic dikes share some characteristics with arc magmas, but are distinctly enriched in Ag and W, which can be either a magma source signature, or a result of intra-channel hybridization by ultramafic wall-rock. Some felsic dikelets show petrographic evidence for such hybridization including the incorporation of resorbed ultramafic mineral phases and micro-xenoliths [96]. The general enrichment of Ildeus rocks in Ag and W (Figure 20) as well as PGE and Au (Figure 19) is consistent with mineralogical data, e.g., presence of native W, Pt, Ag, Au metals and W-Fe-Co-Ti, Ag-Au, Cu-Ag-Au and PGE alloys in both plutonic and metasomatic lithologies (Table 6).

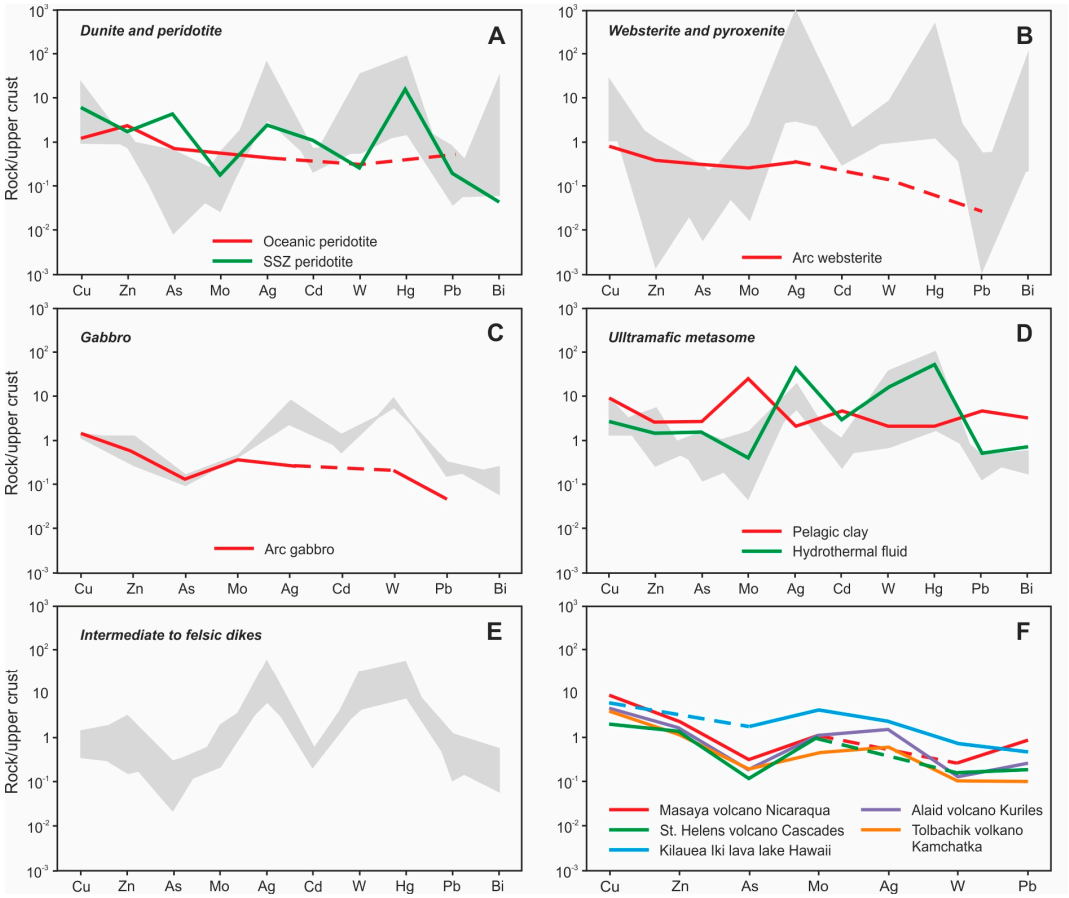

Figure 20. Distribution of siderophile (Mo, W) and chalcophile (Cu, Zn, As, Ag, Cd, Hg, Pb, Bi) elements in magmatic and metasomatic rocks from the Ildeus mafic–ultramafic complex (**A**–**E**) and

modern lavas from volcanic arcs and oceanic islands (**F**). Data for comparison: variably serpentinized oceanic peridotites (Ag, As, Pb, Cd, Cu and Zn from [120]; Hg and Bi from [121]; Mo from [122]; W from [123]); supra-subduction zone (SSZ) peridotite, arc websterite and arc gabbro from [124]; pelagic clay sediment [98]; hypothetical hydrothermal fluid (Zn, Pb, W from [125]; Mo, Cu, As from [126]; Hg from [127]; Ag from [128]); oceanic basalt glasses from the Kilauea Iki lava lake [129]; arc volcanic rocks from the Andes [130], Masaya volcano, Nicaragua [116], Mt. St. Helens, Cascades [116]; Alaid volcano, Kuriles [116], Tolbachik volcano, Kamchatka [116], Setouchi high-Mg andesite (HMA) from SW Japan [119]. Normalized values for the upper continental crust are from [97].

Variations in Cu and Ag in the Ildeus complex appear to further emphasize the importance of the fluid-controlled behavior of certain chalcophile elements in the Mesozoic Stanovoy subduction zone. Most Ildeus plutonic rocks display very low Cu/Ag ratios (<500) that plot between the Cu/Ag ratio in the average bulk continental crust (Cu/Ag = 482) and in reconstructed composite hydrothermal fluid (Cu/Ag = 93) (Figure 21a).

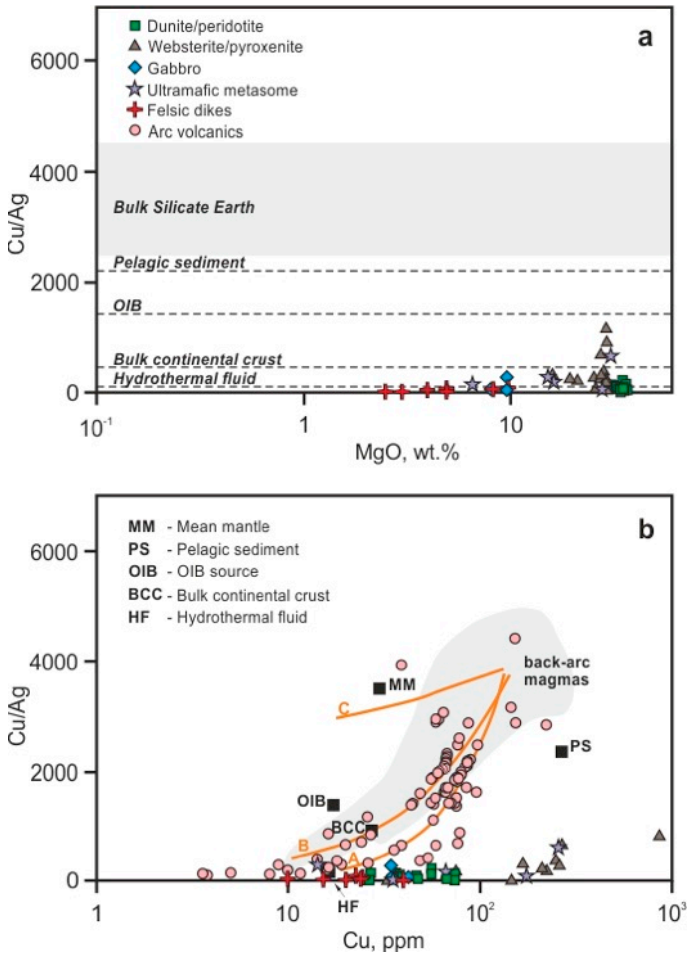

Figure 21. Variation in Cu/Ag ratio versus MgO (wt.%) (**a**) and Cu (ppm) (**b**) in plutonic and metasomatic rocks and felsic dikes from the Ildeus mafic–ultramafic complex compared with other subduction-related rocks (arc volcanics and back-arc magmas) and average Cu/Ag values for mean mantle [131–133], ocean island basalt (OIB) source [129], pelagic sediment [98], bulk continental crust [97] and hydrothermal fluid [126,128]. Grey-shaded field for back-arc magmas on (**b**) is from [133]. Data for arc volcanics are from [130]. Solid lines A, B and C show modeled fractionation trends of sulfide-saturated magmas [133]: (A) monosulfide solid solution (MSS)-silicate melt with D_{Cu} of 400 and D_{Ag} of 40; (B) MSS-silicate melt with D_{Cu} of 480 and D_{Ag} of 192 (equivalent to 80% MSS + 20% coexisting sulfide liquid); (C) sulfide melt–silicate melt with D_{Cu} of 900 and D_{Ag} of 800. Details of used models and partition coefficients can be found in [131].

Since Cu/Ag is only little affected during the melt–peridotite interaction and sulfide-involved fractionation of mantle-derived primary magmas, the very low and reasonably constant Cu/Ag ratio in Ildeus rocks, which is so dramatically different from mantle values of >2000 (mean mantle Cu/Ag = 3500; [93]), suggest a hydrothermal fluid-controlled crustal environment for their formation (Figure 21a). Based on the co-variation in Cu/Ag ratio and MgO (wt.%), we can also rule out any substantial involvement for the monosulfide solid solution (MSS) in the fractionation of Ildeus primary melt at the arc plutonic roots as MSS preferentially retains Cu, relative to Ag, thus severely affecting the resultant Cu/Ag ratio [131]. This is confirmed by the Cu/Ag-Cu systematics, where all Ildeus samples plot at very low Cu/Ag values below the differentiation trends for back-arc and volcanic arc magmas involving MSS fractionation (Figure 21b).

The Cu/Ag-Cu systematics in Ildeus plutonic rocks compared to back-arc and volcanic arc magmas (Figure 21b) show that Ildeus rocks plot at the low-Cu/Ag end of differentiation trends of subduction-zone magmas relatively close to the composite hydrothermal fluid (Cu/Ag = 93; Cu = 16.7 ppm). Broad variations in Cu content of Ildeus plutonic and metasomatic rocks as well as the later-stage felsic dikes (Cu = 10–860 ppm) suggest the accumulation of Cu-sulfides during both magmatic differentiation in the lower sub-arc crust and metasomatic reactions in the collision-related upper crust. This is supported by the presence of primary chalcopyrite and bornite in high-temperature (Figure 14G; [69]) and secondary chalcopyrite, digenite and chalcocite in low-temperature (Figure 14H,I; [69]) rock-forming silicates (Table 6). Since Cu and Ag contents in Ildeus plutonic rocks do not show any significant systematic variations with fractional crystallization indices such as MgO (Figure 21a), we assume that the Cu/Ag ratio in the Ildeus system is to a significant extent controlled by the sulfur-saturated hydrothermal fluid enriched in certain siderophile (W, Pt, Au) and chalcophile (Cu, Ag) metals. We also propose that during later-stage metasomatism, the chalcophile element signature of a possible mantle source was altered by metasomatic reactions with a high fluid/rock ratio. Consequently, the original metal characteristics of Ildeus primary melt can be reconstructed only with the assistance of micro-metallogenic studies of metal inclusions in host high-temperature silicate minerals. In addition, the interaction between Ildeus plutonic rocks and slab melts can also substantially lower Cu/Ag ratios of the former, as slab melts (e.g., lavas from the submarine Piip volcano in the western Aleutian arc) are characterized by low Cu concentrations of 10–30 ppm and Cu/Ag values of 200–460 compared with the bulk continental crust [134].

Behavior of ore metals in the Ildeus plutonic system can be further evaluated using relationships of volatile siderophile element tungsten with some incompatible high-field strength elements such as Ta, Th and U (Figure 22). Tungsten is highly incompatible in magmatic processes (even in comparison with Th, U and Ta) and consequently enriched in the continental crust (~1 ppm; [97]) relative to the mantle (~12 ppb; [135]). It was also originally deemed to be immobile in subduction zones [116], but recent high-precision analysis of bulk tungsten concentrations and its isotopes in various arc-related rocks indicate that W (along with Mo) can be mobilized by subduction fluids, although to a different degree [117,118,136]. It is important to emphasize that W/Th, W/Ta and, to a lesser extent, W/U ratios are sensitive indicators of the amount of fluid phase, since W always strongly partitions into the fluid independently of fO_2 and salinity [136]. Tungsten is also enriched relative to Th, U and Ta in altered mafic oceanic crust and variably serpentinized abyssal peridotites, suggesting strong W concentration during seafloor serpentinization and late-stage oxidative seawater alteration [123]. Peridotite hybridization by silicic sediment melts is also capable of producing high W/HFSE ratios in mantle sources of some arc magmas [117,119].

Plutonic and metasomatic rocks from the Ildeus complex display elevated W concentrations with W/U, W/Th and W/Ta ratios ten to hundred times higher than the mean mantle value (Figure 22). W/U ratios in most peridotites, pyroxenites, ultramafic metasomes and felsic dikes cluster around average hydrothermal fluid values of W/U = 113; [137]), substantially above (>10) W/U values for the primitive mantle (W/U = 0.62 ± 0.19; [138])

and bulk silicate earth (BSE; W/U = 0.65 ± 0.45; [139]). Ultramafic metasomes display the largest range of W/U ratios (1–1140; Figure 22a), possibly due to the diverse W behavior under hydrothermal conditions. Reifenröther et al. [123] suggested that W is enriched during serpentinization and seawater interaction, but depleted in silicic metasomatic reactions involving the formation of talc. This is consistent with our petrographic observations, as the sample with a W/U ratio of 1.1 contains a substantial amount of talc.

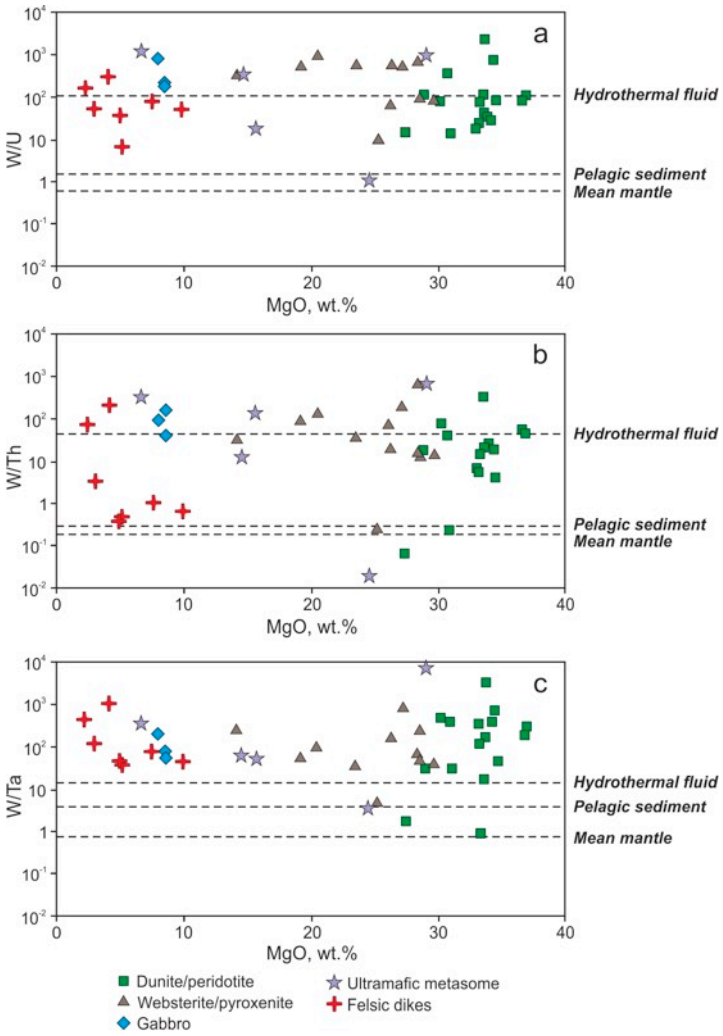

Figure 22. MgO (wt.%) versus W/U (**a**), W/Th (**b**) and W/Ta (**c**) in plutonic and metasomatic rocks and felsic dikes from the Ildeus complex. Average W-U-Th-Ta ratios in the mean mantle (W/U = 0.65; W/Th = 1.54; W/Ta = 113) are from [138,139]; pelagic sediment (W/U = 1.54; W/Th = 0.31; W/Ta = 4) from [98]; hydrothermal fluid (W/U = 113; W/Th = 47; W/Ta = 15) from [137].

Although several peridotites and ultramafic metasomes from the Ildeus complex have W/Th and W/Ta ratios similar to or even below typical mantle values (W/Th = 0.19; W/Ta = 0.2) [93,129], most ultramafic rocks are grouped (W/Th = 4–368; W/Ta = 5–820) around W/HFSE ratios characteristic of hydrothermal fluids, e.g., W/Th of ~47 and W/Ta of ~15 (Figure 22b and c, respectively). The difference between the mantle and pelagic sediment (potential contaminant of mantle sources and primitive subduction-related melts) W-Th-Ta signature and the Ildeus complex is so significant that, in our opinion, it can only be attributed to extensive fluid–rock interactions during emplacement of the Ildeus intrusion in the uppermost crust beneath the Stanovoy suture [69]. Intense metasomatism with a high fluid/rock ratio is characteristic of subduction zone environments in general [140,141]. Additional metasomatic changes can be linked to the post-collisional adakitic dikes, which

display W/Th and W/Ta ratios intermediate between the hydrothermal fluid and pelagic sediment values (Figure 22b,c). The presence of native tungsten and tungsten alloys in high-temperature minerals of the Ildeus intrusion potentially signal that primary Ildeus melt carried a considerable amount of this siderophile metal, which was introduced into its hypothetical mantle wedge source by pelagic sediment-derived fluids. This appears to be a generally plausible mechanism for W enrichment in sub-arc mantle sources as pelagic clays contain an average of 4 ppm of tungsten [98] compared to the available W estimates of 10 ± 3 ppb [138] and 13 ± 10 ppb for the primitive mantle and 3.0 ± 2.3 ppb for the depleted MORB mantle [139]. This is also consistent with the presence of native W and Mn-W alloys in mantle wedge peridotite xenoliths from the Avachinsky volcano in the Kamchatka arc [68].

5.4. Two-Stage Model for Magmatic–Hydrothermal Metal Transport at Arc Plutonic Roots

The geochemical and mineralogical data presented above allow us to link some siderophile and chalcophile element enrichments in the Ildeus complex to different stages of fluid–melt and fluid–rock interactions in the evolving plutonic plumbing system beneath the Mesozoic Stanovoy convergent margin.

Petrologic and geochemical reconstructions [69,70,83,96] indicate that Ildeus ultramafic–mafic cumulates were produced through polybaric fractionation of the mantle-derived mafic melt at the base of the Mesozoic continental arc. The crystallization of intercumulus amphibole, occurrence of equant olivine inclusions in pyrrhotite (Figure 14E) along with the presence of Cu-Ag-Pb-Sn halides (in addition to NaCl in and KCl microinclusions in olivine and amphibole [69]) in magmatic-textured silicates (Figure 13) suggest the formation of Ildeus ultramafic cumulates in the presence of high-temperature H-S-Cl fluid. Based on the early precipitation of base metal sulfides, magmatic fluid was enriched in sulfide over sulfate sulfur and, therefore, relatively unoxidized [33]. Although some early olivine and orthopyroxene contain minute inclusions of barite (Figure 18A–C), this most probably had an overall negligible effect on the redox conditions in the Ildeus melt-fluid system as even sulfate-saturated basaltic magmas are characterized by an oxygen fugacity below + 2 ΔQFM [142]. A reduced fluid characteristic during Ildeus magmatic differentiation is also implied by the presence of native siderophile (W, Pt, Au) and chalcophile (Bi, Zn, Cu [69,96]) metals and their alloys (W-Fe, W-Co-Ti, Cu-Ag-Au, etc.) in high-temperature silicate minerals (Figures 8–12). These metallic phases are comparable to Cu-Ni-Co-Fe metal assemblages formed in some Alpine peridotites and ophiolitic chromitites under highly reducing conditions (fO_2 values of 4 log units or more below QFM) in the presence of CH_4-H_2-bearing saline aqueous fluids [143,144]. This is consistent with experimentally determined intrinsic oxygen fugacity values of −2 to −4 ΔQFM for platinum and PGE alloys in layered mafic–ultramafic intrusions [145,146]. Berdnikov et al. [70,147] proposed on the basis of phase equilibria that Cu-Ag-Au alloys in igneous systems are formed under strongly reduced conditions below the QFM buffer. The geochemical enrichment of Ildeus ultramafic cumulates in W, Pt, Au and Ag relative to the upper continental crust combined with metal inclusions in high-temperature minerals imply that reduced high-temperature fluids were enriched in some siderophile (W, Pt, Au) and chalcophile (Cu, Zn, Ag, Bi) elements most probably inherited from their sub-arc mantle sources.

Mantle-wedge-derived peridotite xenoliths from arc volcanoes are enriched in PGE and Au compared to depleted MORB mantle and contain micro-inclusions of native Fe, Pt, Au, Cu, Zn, Pb and Bi along with Cu-Ag-Au and Cu-Sn-Zn alloys hosted in primary olivine and orthopyroxene [2–4,68]. Petrologic reconstructions suggest that metals were introduced into the sub-arc mantle wedge by slab-derived fluids under relatively low-oxygen-fugacity conditions (−2 to +1 ΔQFM; [68]). Reduced H-S-Cl fluid sourced from subducted serpentinite through buffering mineral reactions along the slab–mantle interface [148,149] fluxes the overlying mantle wedge with sulfur and halogens (Cl, Br, I) [36,37,150] as well as volatile siderophile (W, Mo) and chalcophile (Cu, Zn, Pb, Bi) elements. Saline aqueous fluids will also mobilize and transport noble metals [23,26,35–37,151] into the mantle wedge peridotite

to create a metal-rich sub-arc mantle source represented, for example, by veined peridotite xenoliths from Kamchatka and some Melanesian volcanic arcs [2–4,68]. Fluid-fluxed melting of the metal-rich mantle source generates reduced early-arc and fore-arc melts [152,153], which will produce upon differentiation arc root plutonic suites similar in mineralogy and metal tenor to the IIdeus ultramafic complex. Slab- and sediment-derived melts are also enriched in some siderophile and chalcophile elements [64,117,119,134] possibly contributing to the W and Ag anomalies in plutonic arc root systems (Figure 20) as suggested by Cu-Ag and W-U-Th-Ta systems (Figures 21 and 22, respectively). Geochemical data from the Cyprus and Papua New Guinea boninites indicate that metalliferous sediments in the subducted slab contribute substantial amounts of W, Mo and Zn to slab-derived fluids, which can be further incorporated into the mantle sources of arc magmas [154].

Metal endowment created at the Triassic arc plutonic roots during magmatic differentiation of the primary Ildeus melt was further upgraded through hydrothermal fluid–rock interactions within the upper crust of the Cretaceous Stanovoy collided margin [69,70,96]. Tectonic exhumation of the Ildeus core plutonic complex within the attenuated crust was accompanied by intense circulation of oxidized aqueous solutions rich in chlorine and sulfate ions. This is consistent with the common presence of Cu-Ag-chlorides (Figure 13G–I) and barite (Figure 18D–F) in metasomatic minerals such as chlorite, orthoclase, epidote and serpentine (Table 6). It is important to emphasize that Cu-Ag-Cl compounds are typically found in low-temperature volcanic gas emissions and mineralizing epithermal environments [96,114,128,155,156], associated with oxidizing fumarolic vents [157,158]. The presence of interstitial non-stoichiometric bismuth chloride (Figure 13F) with a melting temperature of 234 °C [96] suggests temperatures above 200 °C for the later-stage metasomatic fluids, which is consistent with experimental data for Bi-chloride complexes in low-temperature hydrothermal solutions [159]. The abundance of barite in metasomatic minerals (Figure 18D–F; Table 6; [69,96]) and the widespread replacement of primary sulfides and barite by magnetite (Figures 14A and 18C) attest to the general oxidized nature (possibly several log units above the QFM buffer) of late-stage fluids in the Ildeus system [69,70,83,96]. This is consistent with the prevailing oxidizing nature of arc volcanic gases and shallow, low-temperature solutions beneath arc volcanoes [9,113,158,160].

The distribution of chalcophile and siderophile elements in ultramafic metasomes from the Ildeus arc root system demonstrates their enrichment in Cu, Zn, Ag, W and Hg and depletion in As, Mo, Cd and Pb, similar to the distribution of these metals in some shallow, low-temperature hydrothermal fluids (Figure 20D). Metasomatic samples from the Ildeus complex display very low Cu/Ag ratios (typically under 500) and highly variable Cu contents resulting from a dynamically changing rock/fluid ratio during shallow hydrothermal reactions. This is consistent with the sporadic formation of copper-rich secondary phases, such as digenite and chalcocite (Figure 14I) in some Ildeus metasomes [69,96]. Ultramafic metasomes display variable, but generally high W contents (1.37–74.75 ppm; Table 3) and, with an exception of sample 30243 (Table 3), high W/U, W/Th and W/Ta ratios (Figure 22). This is consistent with the elevated tungsten mobility in low-temperature (200–350 °C) hydrothermal fluids [161,162] possibly enhanced by the presence of chloride complexes [163–165]. These shallow hydrothermal fluids were enriched in gold (Figure 19), copper and silver (Figure 20D) as demonstrated by the presence of native Au (Figure 9C) along with Au-Ag (Figure 9E,F) and Cu-Ag (Figure 11D–F) alloys in secondary silicates within the Ildeus plutonic system. The appearance of telluride minerals in hydrothermal assemblages [69,96] suggests that the later-stage hydrothermal reactions occurred within the shallow oxidized epithermal environment in the attenuated crust beneath the Mesozoic Stanovoy collided margin.

6. Conclusions

1. The Ildeus complex was formed through the fractionation of olivine, orthopyroxene, clinopyroxene and spinel from hydrous HFSE-depleted mafic melt within a plutonic

root system of the Mesozoic Stanovoy continental margin. Later-stage interstitial plagioclase and amphibole crystallized from an evolved residual melt.

2. The Ildeus complex was subjected to large-scale metasomatism resulting in the formation of ultramafic (talc-chlorite-serpentine) and quartz-rich metasomes. Some of the quartz-rich metasomatic zones with quartz-carbonate-adularia veins are spatially associated with later-stage adakitic veins and dikes.
3. Ultramafic cumulates contain magmatic base metal sulfides (pentlandite, Co-pentlandite, pyrrhotite, chalcopyrite, composite Ni-Co-Cu-Zn-Fe sulfides), siderophile native metals (W, Pt, Au), W-Co-Ti, Fe-Cu-Pt, Ni-Cu-Zn-Ag alloys in association with Ag-chloride, Ag-iodide and Cu-Ag-sulfide. Ildeus metasomes include heazlewoodite, digenite, chalcocite, relic pentlandite and Ni-pyrrhotite, galena, sphalerite, pyrite, acanthite, composite Cu-Zn-Pb-As sulfides, sulfosalts, Pb-Ag-tellurides along with Cu-Ag-chloride and abundant barite.
4. High-temperature metal assemblages were formed during the polybaric magmatic differentiation of mafic melt in the presence of reduced H-S-Cl-rich fluids. This metal-rich melt was sourced in a depleted sub-arc mantle wedge fertilized by slab/sediment-derived fluids or melts enriched in W, Pt, Au, Ag, Cu and Zn. Metal assemblages hosted in secondary silicates were formed in the presence of oxidized low-*P-T* fluids enriched in chlorine, sulfate and Pb, Zn, Sb, Sn, Au, Ag, Se and Te.
5. A two-stage model of metal transport in subduction zones is proposed, which involves the magmatic fractionation of high-temperature siderophile and chalcophile metals and their alloys from fertile mantle-wedge-derived reduced melts followed by the large-scale resuscitation and metal upgrade of the plutonic root system in the shallow oxidized epithermal environments of the subduction/collision-related upper crust.

Author Contributions: Conceptualization, P.K., N.B. and N.K.; methodology, P.K. and N.B.; software, N.B. and N.K.; formal analysis, N.B., V.K. and I.A.; investigation, P.K., N.B., N.K., V.K. and I.A.; resources, P.K. and N.B.; data curation, P.K., N.B. and N.K.; writing—original draft preparation, P.K., N.B. and N.K.; writing—review and editing, P.K. and N.B.; visualization, N.B. and N.K.; supervision, P.K. and N.B.; project administration, P.K. and N.B.; funding acquisition, P.K. and N.B. All authors have read and agreed to the published version of the manuscript.

Funding: This research was performed in the context of the Government Assignment to the Institute of Tectonics and Geophysics, Far East Branch, Russian Academy of Sciences with financial support from the Russian Science Foundation, grant 22-17-00023.

Data Availability Statement: Data are available upon request from the senior author.

Acknowledgments: We wish to thank Tore Birkeland, Chairman of Khingan Minerals AS (Oslo, Norway) for his continuous support of this project. We are grateful to Oleg Alekseenko, Mikhail Zhuravlev, Yuri Skornyakov, Yuri Taltykin, Alexander Belousov and Ekaterina Konovalova for their help in the acquisition of geophysical and geological information on the Ildeus intrusion and collection of grab and drill core samples. We also acknowledge three anonymous journal reviewers, who have greatly helped to improve the original version of this manuscript.

Conflicts of Interest: The authors declare no conflict of interest.

References

1. Watson, J.V. Metallogenesis in relation to mantle heterogeneity. *Philos. Trans. R. Soc. Lond. A* **1980**, *297*, 347–352.
2. McInnes, B.I.A.; McBride, J.S.; Evans, N.J.; Lambert, D.D.; Andrew, A.S. Osmium isotope constraints on ore metal recycling in subduction zones. *Science* **1999**, *286*, 512–516. [CrossRef]
3. Kepezhinskas, P.; Defant, M.J.; Widom, E. Abundance and distribution of PGE and Au in the island-arc mantle: Implications for sub-arc metasomatism. *Lithos* **2002**, *60*, 113–128. [CrossRef]
4. Widom, E.; Kepezhinskas, P.; Defant, M.J. The nature of metasomatism in the sub-arc mantle wedge: Evidence from Re-Os isotopes in Kamchatka peridotite xenoliths. *Chem. Geol.* **2003**, *196*, 283–306. [CrossRef]
5. Richards, J.P. Postsubduction porphyry Cu-Au and epithermal Au deposits: Products of remelting of subduction-modified lithosphere. *Geology* **2009**, *37*, 247–250. [CrossRef]

6. Pettke, T.; Oberli, F.; Heinrich, C.A. The magma and metal source of giant porphyry-type ore deposits, based on lead isotope microanalysis of individual fluid inclusions. *Earth Planet. Sci. Lett.* **2010**, *296*, 267–277. [CrossRef]
7. Wilkinson, J.J. Triggers for the formation of porphyry ore deposits in magmatic arcs. *Nat. Geosci.* **2013**, *6*, 917–925. [CrossRef]
8. Saunders, J.E.; Pearson, N.J.; O'Reilly, S.Y.; Griffin, W.L. Gold in the mantle: A global assessment of abundance and redistribution processes. *Lithos* **2018**, *322*, 376–391. [CrossRef]
9. Richards, J.P. Magmatic to hydrothermal metal fluxes in convergent and collided margins. *Ore Geol. Rev.* **2011**, *40*, 1–26. [CrossRef]
10. Burnham, C.W. Magmas and hydrothermal fluids. In *Geochemistry of Hydrothermal Ore Deposits*, 2nd ed.; Barnes, H.L., Ed.; John Wiley & Sons: New York, NY, USA, 1979; pp. 71–136.
11. Sobolev, V.S.; Dobretsov, N.L.; Glebovitsky, V.A.; Kepezhinskas, K.B.; Khlestov, V.V.; Sokolov, Y.M.; Turchenko, S.I. Petrologic and physic-cheemical aspects of metamorphogenic ore mineralization. *Bull. Geol. Surv. Finl.* **1980**, *37*, 84–97.
12. Kepezhinskas, K.B.; Tomilenko, A.A. Composition of fluid inclusions in mineralized versus barren cordierite-anthophyllite metamorphic rocks. *Proc. All-Union Miner. Soc.* **1982**, *111*, 546–551.
13. Hedenquist, J.W.; Lowenstern, J.B. The role of magmas in the formation of hydrothermal ore deposits. *Nature* **1994**, *370*, 519–527. [CrossRef]
14. Glasby, G.P. The relation between ore-deposit formation and subduction: Mass balance considerations. *Isl. Arc* **1996**, *5*, 396–406. [CrossRef]
15. Cartright, I.; Oliver, N.H.S. Metamorphic fluids and their relationship to the formation of metamorphosed and metamorphogenic ore deposits. *Rev. Econ. Geol.* **2000**, *11*, 81–96.
16. Hattori, K.; Keith, J.D. Conribution of mafic melt to porphyry copper mineralization: Evidence from Mount Pinatubo, Philippines, and Bingham Canyon, Utah, USA. *Mineral. Depos.* **2001**, *36*, 799–806. [CrossRef]
17. Mungall, J.E. Roasting the mantle: Slab melting and the genesis of major Au and Au-rich Cu deposits. *Geology* **2002**, *30*, 915–918. [CrossRef]
18. Richards, J. Tectono-magmatic precursors for porphyry Cu-(Mo-Au) deposit formation. *Econ. Geol.* **2003**, *98*, 1515–1533. [CrossRef]
19. Mungall, J.E.; Hanley, J.J.; Arndt, N.T.; Debecdelievre, A. Evidence from meimechites and other low-degree mantle melts for redox controls on mantle-crust fractionation of platinum-group elements. *Proc. Natl. Acad. Sci. USA* **2006**, *103*, 12695–12700. [CrossRef]
20. Cooke, D.R.; Hollings, P.; Walshe, J.L. Giant porphyry deposits: Characteristics, distribution, and tectonic controls. *Econ. Geol.* **2005**, *100*, 801–818. [CrossRef]
21. Halter, W.E.; Heinrich, C.A.; Pettke, T. Magma evolution and the formation of porphyry Cu-Au ore fluids: Evidence from silicate and sulfide melt inclusions. *Miner. Depos.* **2005**, *39*, 845–863. [CrossRef]
22. Lee, C.-T.A.; Luffi, P.; Chin, E.J.; Bouchet, R.; Dasgupta, R.; Morton, D.M.; Le Roux, V.; Yin, Q.-Z.; Jin, D. Copper systematics in arc magmas and implications for crust-mantle differentiation. *Science* **2012**, *336*, 64–68. [CrossRef] [PubMed]
23. Li, J.-L.; Gao, J.; John, T.; Klemd, R.; Su, W. Fluid-mediated metal transport in subduction zones and its link to arc-related giant ore deposits: Constraints from a sulfide-bearing HP vein in lawsonite eclogite (Tianshan, China). *Geochim. Cosmochim. Acta* **2013**, *120*, 326–362. [CrossRef]
24. Grondahl, C.; Zajacz, Z. Magmatic controls on the genesis of porphyry Cu-Mo-Au deposits: The Bingham Canyon example. *Earth Planet. Sci. Lett.* **2017**, *480*, 53–65. [CrossRef]
25. Wang, Y.-Y.; Xiao, Y. Fluid-controlled element transport and mineralization in subduction zones. *Solid Earth Sci.* **2018**, *3*, 87–104. [CrossRef]
26. Audétat, A.; Edmonds, M. Magmatic-hydrothermal fluids. *Elements* **2020**, *16*, 401–406. [CrossRef]
27. De Hoog, J.C.M.; Mason, P.R.D.; van Bergen, M.J. Sulfur and chalcophile elements in subduction zones: Constraints from a laser ablation ICP-MS study of melt inclusions from Galunggung Volcano, Indonesia. *Geochim. Cosmochim. Acta* **2001**, *65*, 3147–3164. [CrossRef]
28. Simon, A.C.; Frank, M.R.; Pettke, T.; Candela, P.A.; Piccoli, P.M.; Heinrich, C.A. Gold partitioning in melt-vapor-brine systems. *Geochim. Cosmochim. Acta* **2005**, *69*, 3321–3335. [CrossRef]
29. Zajacz, Z.; Halter, W. Copper transport by high temperature, sulfur-rich magmatic vapor: Evidence from silicate melt and vapor inclusions in a basaltic andesite from the Villarrica volcano (Chile). *Earth Planet. Sci. Lett.* **2009**, *282*, 115–121. [CrossRef]
30. Pokrovski, G.S.; Borisova, A.Y.; Harrichoury, J.-C. The effect of sulfur on vapor-liquid fractionation of metals in hydrothermal systems. *Earth Planet. Sci. Lett.* **2008**, *266*, 345–362. [CrossRef]
31. Mungall, J.E.; Brenan, J.M. Partitioning of platinum-group elements and Au between sulfide liquid and basalt and the origins of mantle-crust fractionation of the chalcophile elements. *Geochim. Cosmochim. Acta* **2014**, *125*, 265–289. [CrossRef]
32. Lecumberri-Sanchez, P.; Steele-MacInnis, M.; Wies, P.; Driesner, T.; Bodnar, R.J. Salt precipitation in magmatic-hydrothermal systems associated with upper crustal plutons. *Geology* **2015**, *43*, 1063–1066. [CrossRef]
33. Canil, D.; Fellows, S.A. Sulphide-sulphate stability and melting in subducted sediment and its role in arc mantle redox and chalcophile cycling in space and time. *Earth Planet. Sci. Lett.* **2017**, *470*, 73–86. [CrossRef]
34. Li, Y.; Feng, L.; Kiseeva, E.S.; Gao, Z.; Guo, H.; Du, Z.; Wang, F.; Shi, L. An essential role for sulfur in sulfide-silicate melt partitioning of gold and magmaic gold transport at subduction settings. *Earth Planet. Sci. Lett.* **2019**, *528*, 115850. [CrossRef]

35. Tagirov, B.R.; Filimonova, O.; Trigub, A.L.; Akinfiev, N.N.; Nickolsky, M.S.; Kvashnina, K.O.; Chareev, D.A.; Zotov, A.V. Platinum transport in chloride-bearing fluids and melts: Insights from in situ X-ray absorption spectrometry and thermodynamic modeling. *Geochim. Cosmochim. Acta* **2019**, *254*, 86–101. [CrossRef]
36. Grondahl, C.; Zajacz, Z. Sulfur and chlorine budgets control the ore fertility of arc magmas. *Nat. Commun.* **2022**, *13*, 4218. [CrossRef]
37. Castillo, P.R. Arc magmatism and porphyry-type ore deposition are primarily controlled by chlorine from seawater. *Chem. Geol.* **2022**, *589*, 120683. [CrossRef]
38. Alex, A.; Zajacz, Z. The solubility of Cu, Ag and Au in magmatic sulfur-bearing fluids as a function of oxygen fugacity. *Geochim. Cosmochim. Acta* **2022**, *330*, 93–115. [CrossRef]
39. Nadeau, O.; Williams-Jones, A.E.; Stix, J. Sulphide magma as a source of metals in arc-related magmatic hydrothermal ore fluids. *Nature Geosci.* **2010**, *3*, 501–505. [CrossRef]
40. Li, Y.; Audétat, A. Gold solubility and partitioning between sulfide liquid, monosulfide solid solution and hydrous mantle melts: Implications for the formation of Au-rich magmas and crust-mantle differentiation. *Geochim. Cosmochim. Acta* **2013**, *118*, 247–262. [CrossRef]
41. Kiseeva, E.S.; Wood, B.J. A simple model for chalcophile element partitioning between sulphide and silicate liquids with geochemical applications. *Earth Planet. Sci. Lett.* **2013**, *383*, 68–81. [CrossRef]
42. Robertson, J.C.; Barnes, S.J.; Le Vaillant, M. Dynamics of magmatic sulphide droplets during transport in silicat melts and implications for magmatic sulphide ore formation. *J. Petrol.* **2015**, *56*, 2445–2472. [CrossRef]
43. Kutyrev, A.; Zelenski, M.; Nekrylov, N.; Savelyev, D.; Kontonikas-Charos, A.; Kamenetsky, V.S. Noble metals in arc basaltic magmas worldwide: A case study of modern and pre-historic lavas of the Tolbachik volcano, Kamchatka. *Front. Earth Sci.* **2021**, *9*, 1199. [CrossRef]
44. Sinyakova, E.; Kosyakov, V.I.; Borisenko, A.S.; Karmanov, N.S. Behavior of noble metals during fractional crystallization of Cu-Fe-Ni-(Pt, Pd, Rh, Ir, Ru, Ag, Au, Te) sulfide melts. *Russ. Geol. Geophys.* **2019**, *60*, 642–651. [CrossRef]
45. Holwell, D.A.; Fiorentini, M.L.; Knott, T.R.; McDonald, I.; Blanks, D.E.; Campbell McCuaig, T.; Gorczyk, W. Mobilization of deep crustal sulfide melts as a first order control on upper lithospheric metallogeny. *Nat. Commun.* **2022**, *13*, 573. [CrossRef] [PubMed]
46. Shinohara, H.; Hedenquist, J.W. Constraints on magma degassing beneath the Far Southeast porphyry Cu-Au deposit, Philippines. *J. Petrol.* **1997**, *38*, 1741–1752. [CrossRef]
47. Yang, K.; Scott, S.D. Magmatic degassing of volatiles and ore metals into a hydrothermal system on the modern sea floor of the Eastern Manus back-arc basin, Western Pacific. *Econ. Geol.* **2002**, *97*, 1079–1100. [CrossRef]
48. Rohrlach, B.D.; Loucks, R.R. Multi-million-year cyclic ramp-up of volatiles in a lower crustal magma reservoir trapped below the Tampakan copper-gold deposit by Mio-Pliocene crustal compression in the southern Philippines. In *Super Porphyry Copper and Gold Deposits: A Global Perspective*; Porter, T.M., Ed.; PGC Publishing: Toronto, ON, Canada, 2005; Volume 2, pp. 369–407.
49. Fulignati, P.; Kamenetsky, V.S.; Marianelli, P.; Sbrana, A.; Meffre, S. First insights on the metallogenic signature of magmatic fluids exsolved from the active magma chamber of Vesuvius (AD 79 "Pompei" eruption). *J. Volcanol. Geotherm. Res.* **2011**, *200*, 223–233. [CrossRef]
50. Costa, S.; Fulignati, P.; Gioncada, A.; Pistolesi, M.; Bosch, D.; Bruguier, O. Tracking metal evolution in arc magmas: Insights from the active volcano of La Fossa, Italy. *Lithos* **2021**, *380–381*, 105851. [CrossRef]
51. Blundy, J.; Afanasyev, A.; Tattitch, B.; Sparks, S.; Melnik, O.; Utkin, I.; Rust, A. The economic potential of metalliferous sub-volcanic brines. *Royal Soc. Open Sci.* **2021**, *8*, 202192. [CrossRef]
52. Tattitch, B.; Chelle-Michou, C.; Blundy, J.; Loucks, R.R. Chemical feedbacks during magma degassing control chlorine partitioning and metal extraction in volcanic arcs. *Nat. Commun.* **2021**, *12*, 1774. [CrossRef]
53. Gualda, G.A.; Anderson, A.T., Jr. Magnetite scavenging and the buoyancy of bubbles in magmas. Part 1: Discovery of a pre-eruptive bubble in Bishop rhyolite. *Contrib. Mineral. Petrol.* **2007**, *153*, 733–742. [CrossRef]
54. Mungall, J.E.; Brenan, J.M.; Godel, B.; Barnes, S.J.; Gaillard, F. Transport of metals and sulphur in magmas by flotation of sulphide melt on vapour bubbles. *Nat. Geosci.* **2015**, *8*, 216–219. [CrossRef]
55. Edmonds, M. Flotation of magmatic minerals. *Geology* **2015**, *43*, 655–656. [CrossRef]
56. Knipping, J.L.; Webster, J.D.; Simon, A.C.; Holtz, F. Accumulation of magnetite by flotation on bubbles during decompression of silicate magma. *Sci. Rep.* **2019**, *9*, 3852. [CrossRef] [PubMed]
57. Yao, Z.S.; Mungall, J.E. Flotation mechanism of sulphide melt on vapour bubbles in partially molten magmatic systems. *Earth Planet. Sci. Lett.* **2020**, *542*, 116298. [CrossRef]
58. Heinrich, C.A.; Connolly, J.A.D. Physical transport of magmatic sulfides promotes copper enrichment in hydrothermal ore fluids. *Geology* **2022**, *50*, 1101–1105. [CrossRef]
59. Huber, C.; Bachmann, O.; Vigneresse, J.-L.; Dufek, J.; Parmigiani, A. A physical model for metal extraction and transport in shallow magmatic systems. *Geochem. Geophys. Geosyst.* **2012**, *13*. [CrossRef]
60. Li, P.; Boudreau, A.E. Vapor transport of silver and gold in basaltic lava flows. *Geology* **2019**, *47*, 877–880. [CrossRef]
61. Hunter, E.A.O.; Hunter, J.R.; Zajacz, Z.; Keith, J.D.; Hann, N.L.; Christiansen, E.H.; Dorais, M.J. Vapor transport and deposition of Cu-Sn-Co-Ag alloys in vesicles in mafic volcanic rocks. *Econ. Geol.* **2020**, *115*, 279–301. [CrossRef]
62. Berdnikov, N.; Nevstruev, V.; Kepezhinskas, P.; Astapov, I.; Konovalova, N. Gold in mineralized volcanic systems from the Lesser Khingan Range (Russian Far East): Textural types, composition and possible origins. *Geosciences* **2021**, *11*, 103. [CrossRef]

63. Berdnikov, N.V.; Nevstruev, V.G.; Kepezhinskas, P.K.; Krutikova, V.P.; Konovalova, N.S.; Astapov, I.A. Silicate, Fe-oxide, and Au-Cu-Ag microspherules in ores and pyroclastic rocks of the Kostenga iron deposit, in the Far East of Russia. *Russ. J. Pac. Geol.* **2021**, *15*, 236–251. [CrossRef]
64. Kepezhinskas, P.; Berdnikov, N.; Kepezhinskas, N.; Konovalova, N. Adakites, high-Nb basalts and copper-gold deposits in magmatic arcs and collisional orogens. *Geosciences* **2022**, *12*, 29. [CrossRef]
65. Kepezhinskas, P.; Berdnikov, N.; Konovalova, N.; Kepezhinskas, N.; Krutikova, V.; Kirichenko, E. Native metals and alloys in trachytes and shoshonite from the continental United States and high-K dacite from the Bolivian Andes: Magmatic origins of ore metals in convergent and within-plate tectonic settings. *Russ. J. Pac. Geol.* **2022**, *16*, 405–426. [CrossRef]
66. Locmelis, M.; Fiorentini, M.L.; Rushmer, T.; Arevalo, R., Jr.; Adam, J.; Denyszyn, S.W. Sulfur and metal fertilization of the lower continental crust. *Lithos* **2016**, *244*, 74–93. [CrossRef]
67. Wang, Z.; Jin, Z.; Mungall, J.E.; Xiao, X. Transport of coexisting Ni-Cu sulfide liquid and silicate melt in partially molten perdiotite. *Earth Planet. Sci. Lett.* **2020**, *536*, 116162. [CrossRef]
68. Kepezhinskas, P.; Berdnikov, N.; Kepezhinskas, N.; Konovalova, N. Metals in Avachinsky peridotite xenoliths with implications for redox heterogeneity and metal enrichment in the Kamchatka mantle wedge. *Lithos* **2022**, *412–413*, 106610. [CrossRef]
69. Kepezhinskas, P.K.; Kepezhinskas, N.P.; Berdnikov, N.V.; Krutikova, V.O. Native metals and intermetallic compounds in subduction-related ultramafic rocks from the Stanovoy mobile belt (Russian Far East): Implications for redox heterogeneity in subduction zones. *Ore Geol. Rev.* **2020**, *127*, 127. [CrossRef]
70. Berdnikov, N.; Kepezhinskas, P.; Konovalova, N.; Kepezhinskas, N. Formation of gold alloys during crustal differentiation of convergent zone magmas: Constraints from an Au-rich websterite in the Stanovoy Suture Zone (Russian Far East). *Geosciences* **2022**, *12*, 126. [CrossRef]
71. Heinrich, C.A.; Driesner, T.; Stefánsson, T.; Seward, T.M. Magmatic vapor contraction and the transport of gold from the porphyry environment to epithemal ore deposits. *Geology* **2004**, *32*, 761–764. [CrossRef]
72. Simmons, S.F.; Brown, K.L. Gold in magmatic hydrothermal solutions and the rapid formation of a giant ore deposit. *Science* **2006**, *314*, 288–291. [CrossRef]
73. Saunders, J.A.; Burke, M. Formation and aggregation of gold (electrum) nanoparticles in epithermal ores. *Minerals* **2017**, *7*, 163–174. [CrossRef]
74. Hastie, E.C.G.; Schindler, M.; Kontak, D.J.; Lafrance, B. Transport and coarsening of gold nanoparticles in an orogenic deposit by dissolution-reprecipitation and Ostwald ripening. *Commun. Earth Environ.* **2021**, *2*, 57. [CrossRef]
75. Windley, B.F.; Alexeiev, D.; Xiao, W.; Kröner, A.; Badarch, G. Tectonic models for accretion of the Central Asian Orogenic Belt. *J. Geol. Soc. Lond.* **2007**, *164*, 31–47. [CrossRef]
76. Safonova, I. Juvenile versus recycled crust in the Central Asian Orogenic Belt: Implications from ocean plate stratigraphy, blueschist belts and intraoceanic arcs. *Gondwana Res.* **2017**, *47*, 6–27. [CrossRef]
77. Kepezhinskas, K.B. Structural-metamorphic evolution of Late Proterozoic ophiolites and Precambrian basement in the Central Asian foldbelt of Mongolia. *Precambrian Res.* **1986**, *33*, 209–223. [CrossRef]
78. Jahn, B.-M. The Central Asian Orogenic Belt and growth of the continental crust in the Phanerozoic. *Geol. Soc. Lond. Spec. Publ.* **2004**, *226*, 73–100. [CrossRef]
79. Rosen, O.M.; Fedorovsky, V.S. *Collisional Granitoids and Delamination of the Earth's Crust*; Nauchny Mir: Moscow, Russia, 2001; pp. 1–179. (In Russian)
80. Yi, Z.; Meert, J.G. A closure of the Mongol-Okhotsk ocean by the Middle Jurassic: Reconciliation of paleomagnetic and geological evidence. *Geophys. Res. Lett.* **2020**, *47*, e2020GL088235. [CrossRef]
81. Didenko, A.N.; Kaplun, V.B.; Malyshev, Y.F.; Shevchenko, B.F. The lithospheric structure and Mesozoic geodynamics of the eastern Central Asian fold belt. *Russ. Geol. Geophys.* **2010**, *51*, 629–647. [CrossRef]
82. Donskaya, T.V.; Gladkochub, D.P.; Mazukabzov, A.M.; Ivanov, A.V. Late Paleozoic-Mesozoic subduction-related magmatism at the southern margin of the Siberian continent and the 150 million-year history of the Mongol-Okhotsk Ocean. *J. Asian Earth Sci.* **2013**, *62*, 79–97. [CrossRef]
83. Kepezhinskas, P.; Kepezhinskas, N.; Kamenetsky, V.; Berdnikov, N. Multi-stage magmatic to metamorphic formation of Ni-Co-Cu(Pd) mineralization in a subduction-related setting: A case study of the Ildeus-Lucha intrusive complex (Stanovoy mobile belt, SE Siberia). *Geol. Soc. Am. Abstr. Programs* **2018**, *50*. [CrossRef]
84. Drummond, M.S.; Defant, M.J.; Kepezhinskas, P.K. Petrogenesis of slab-derived trondhjemite-tonalite-dacite/adakite magmas. *Trans. Royal Soc. Edinb. Earth Sci.* **1996**, *87*, 205–215.
85. Defant, M.J.; Kepezhinskas, P. Evidence suggests slab melting in arc magmas. *EOS Trans. Am. Geophys. Union* **2001**, *82*, 65–69. [CrossRef]
86. Kepezhinskas, N.; Kamenov, G.D.; Foster, D.A.; Kepezhinskas, P. Petrology and geochemistry of alkaline basalts and gabbroic xenoliths from Utila Island (Bay Islands, Honduras): Insights into back-arc processes in the Central American Volcanic Arc. *Lithos* **2020**, *352–353*, 105306. [CrossRef]
87. Jin, X.; Zhu, H. Determination of platinum-group elements and gold in geological samples with ICP-MS using sodium peroxide fusion and tellurium co-precipitation. *J. Anal. Atom. Spectrom.* **2000**, *15*, 747–751. [CrossRef]
88. Guillou-Frottier, L.; Burov, E.; Augé, T.; Cloaguen, E. Rheological conditions for emplacement of Ural-Alaskan-type ultramafic complexes. *Tectonophysics* **2014**, *631*, 130–145. [CrossRef]

89. Murray, C. Zoned ultramafic complexes of the Alaskan-type: Feeder pipes of andesitic volcanoes. *Geol. Soc. Am. Mem.* **1972**, *132*, 313–335.
90. Whitney, D.L.; Evans, B.W. Abbreviations for names of rock-forming minerals. *Am. Mineral.* **2010**, *95*, 185–187. [CrossRef]
91. Zimmer, M.M.; Plank, T.; Hauri, E.H.; Yogodzinski, G.M.; Stelling, P.; Larsen, J.; Singer, B.; Jicha, B.; Mandeville, C.; Nye, C.J. The role of water in generating the calc-alkaline trend: New volatile data for Aleutian magmas and a new tholeiitic index. *J. Petrol.* **2010**, *51*, 2411–2444. [CrossRef]
92. Beard, J.S. Characteristic mineralogy of arc-related cumulate gabbros: Implications for the tectonic setting of gabbroic plutons and for andesite genesis. *Geology* **1986**, *14*, 848–851. [CrossRef]
93. McDonough, W.F.; Sun, S.-s. The composition of the Earth. *Chem. Geol.* **1995**, *120*, 223–253. [CrossRef]
94. McCulloch, M.T.; Gamble, J.A. Geochemical and geodynamic constraints on subduction zone magmatism. *Earth Planet. Sci. Lett.* **1991**, *102*, 358–374. [CrossRef]
95. Pearce, J.W.; Peate, D.W. Tectonic implications of the composition of volcanic arc magmas. *Annu. Rev. Earth Planet. Sci.* **1995**, *23*, 251–285. [CrossRef]
96. Kepezhinskas, P.K.; Berdnikov, N.V.; Krutikova, V.O.; Kepezhinskas, N.P.; Astapov, I.A.; Kirichenko, E.A. Silver mineralization in the deep-seated magmatic roots of ancient island arcs: Ildeus ultramafic massif, Stanovoy mobile belt (Russian Far East). *Russ. J. Pac. Geol.* **2023**, *42*, 30–60.
97. Rudnick, R.L.; Gao, S. Composition of the continental crust. *Treatise Geochem.* **2014**, *4*, 1–51.
98. Li, Y.-H.; Schoonmaker, J.E. Chemical composition and mineralogy of marine sediments. *Treatise Geochem.* **2003**, *7*, 1–35.
99. Garuti, G.; Fershtater, G.; Bea, F.; Montero, P.; Pushkarev, E.V.; Zaccarini, F. Platinum-group elements as petrological indicators in mafic-ultramafic complexes of the central and southern Urals: Preliminary results. *Tectonophysics* **1997**, *276*, 181–194. [CrossRef]
100. Parfenov, L.M.; Popeko, L.I.; Tomurtogoo, O. Problems of tectonics of the Mongol-Okhotsk orogenic belt. *Geol. Pac. Ocean* **2001**, *16*, 797–830.
101. Antonov, A.Y. Geochemistry and petrology of Mesozoic-Cenozoic magmatic complexes of the southern framing of the Aldan shield: Geodynamic problems. *Russ. J. Pac. Geol.* **2007**, *1*, 153–175. [CrossRef]
102. Khomich, V.G.; Boriskina, N.G.; Santosh, M. Geodynamics of late Mesozoic PGE, Au, and U mineralization in the Aldan shield, North Asian Craton. *Ore Geol. Rev.* **2015**, *68*, 30–42. [CrossRef]
103. Prokopiev, I.R.; Doroshkevich, A.G.; Ponomarchuk, A.V.; Redina, A.A.; Yegitova, I.V.; Ponomarev, J.D.; Sergeev, S.A.; Kravchenko, A.A.; Ivanov, A.I.; Sokolov, E.P.; et al. U-Pb SIMS and Ar-Ar geochronology, petrography, mineralogy and gold mineralization of the late Mesozoic Amga alkaline rocks (Aldan shield, Russia). *Ore Geol. Rev.* **2019**, *109*, 520–534. [CrossRef]
104. DeBari, S.M.; Coleman, R.G. Examination of the deep levels of an island arc: Evidence from the Tonsina ultramafic-mafic assemblage, Tonsina, Alaska. *J. Geophys. Res.* **1989**, *94*, 4373–4391. [CrossRef]
105. Kepezhinskas, P.K.; Reuber, I.; Tanaka, H.; Miyashita, S. Zoned calc-alkaline plutons in Northeastern Kamchatka, Russia: Implications for the crustal growth in magmatic arcs. *Mineral. Petrol.* **1993**, *49*, 147–174. [CrossRef]
106. Blatter, D.L.; Sisson, T.W.; Hankins, W.B. Crystallization of oxidized, moderately hydrous arc basalt at mid- to lower-crustal pressures: Implications for andesite genesis. *Contrib. Mineral. Petrol.* **2013**, *166*, 861–886. [CrossRef]
107. Melekhova, E.; Blundy, J.; Robertson, R.; Humphreys, M.C.S. Experimental evidence for polybaric differentiation of primitive arc basalt beneath St. Vincent, Lesser Antilles. *J. Petrol.* **2015**, *56*, 161–192. [CrossRef]
108. Zhang, J.; Wang, R.; Hong, J. Amphibole fractionation and its potential redox effect on arc crust: Evidence from the Kohistan arc cumulates. *Am. Mineral.* **2022**, *107*, 1779–1788. [CrossRef]
109. Donaldson, M.J. Redistribution of ore elements during serpentinization and talc-carbonate alteration of some Archean dunites, Western Australia. *Econ. Geol.* **1981**, *76*, 1698–1713. [CrossRef]
110. Walters, J.B.; Cruz-Uribe, A.M.; Marschall, H.R. Isotopic compositions of sulfides in exhumed high-pressure terranes: Implications for sulfur cycling in subduction zones. *Geochem. Geophys. Geosyst.* **2019**, *20*, 3347–3374. [CrossRef]
111. Valetich, M.J.; Mavrogenes, J.; Arculus, R.; Umino, S. Evolution of chalcophile elements in the magmas of the Bonin Islands. *Chem. Geol.* **2019**, *508*, 234–249. [CrossRef]
112. Nadeau, O.; Stix, J.; Williams-Jones, A.E. The behavior of Cu, Zn and Pb during magmatic-hydrothermal activity at Merapi volcano, Indonesia. *Chem. Geol.* **2013**, *342*, 167–179. [CrossRef]
113. Edmonds, M.; Mason, E.; Hogg, O. Volcanic outgassing of volatile trace metals. *Annu. Rev. Earth Planet. Sci.* **2022**, *50*, 79–98. [CrossRef]
114. Naboko, S.I. Volcanic exhalations and products of their reactions. *Trans. Volcanol. Lab.* **1959**, *16*, 1–356. (In Russian)
115. Cook, N.J.; Ciobanu, C.L.; Spray, P.G.; Voudouris, P. and the participants of IGCP-486. Understanding gold-(silver)-telluride-(selenide) mineral deposits. *Episodes* **2009**, *32*, 249–263. [CrossRef]
116. Noll, P.D., Jr.; Newsom, H.E.; Leeman, W.P.; Ryan, J.G. The role of hydrothermal fluids in the production of subduction zone magmas: Evidence from siderophile and chalcophile trace elements and boron. *Geochem. Cosmochim. Acta* **1996**, *60*, 587–611. [CrossRef]
117. König, S.; Münker, C.; Schuth, S.; Garbe-Schönberg, D. Mobility of tungsten in subduction zones. *Earth Planet. Sci. Lett.* **2008**, *274*, 82–92. [CrossRef]
118. Canil, D.; Crockford, P.W.; Rossin, R.; Telmer, K. Mercury in some arc crustal rocks and mantle peridotites and relevance to the moderately volatile element budget of the Earth. *Chem. Geol.* **2015**, *396*, 134–142. [CrossRef]

119. Mazza, S.E.; Stracke, A.; Gill, J.B.; Kimura, J.-I.; Kleine, T. Tracing dehydration and melting of the subducted slab with tungsten isotopes in arc lavas. *Earth Planet. Sci. Lett.* **2020**, *530*, 115942. [CrossRef]
120. Silantyev, S.A.; Kubrakova, I.V.; Tyutyunnik, O.A. Distribution of siderophile and chalcophile elements in serpentinites of the oceanic lithosphere as an insight into the magmatic and crustal evolution of mantle peridotites. *Geochem. Internat.* **2016**, *54*, 1019–1034. [CrossRef]
121. Azer, M.K. Evolution and economic significance of listwaenites associated with Neoproterozoic ophiolites in South Eastern Desert, Egypt. *Geol. Acta* **2013**, *11*, 113–128.
122. Babechuk, M.G.; Kamber, B.S.; Greig, A.; Canil, D.; Kodolányi, J. The behavior of tungsten during mantle melting revisited with implications for planetary differentiation time scales. *Geochim. Cosmochim. Acta* **2010**, *74*, 1448–1470. [CrossRef]
123. Reifenröther, R.; Münker, C.; Paulick, H.; Scheibner, B. Alteration of abyssal peridotites is a major sink in the W geochemical cycle. *Geochim. Cosmochim. Acta* **2022**, *321*, 35–51. [CrossRef]
124. Govorov, I.N.; Ilupin, I.P.; Kharkiv, A.D.; Golubeva, E.D.; Denisov, E.P. *Geochemistry of Deep-Seated Volcanic Rocks and Xenoliths*; Nauka Publishers: Moscow, Russia, 1980; 332p. (In Russian)
125. Codeço, M.S.; Weis, P.; Trumbull, R.B.; Van Hinsberg, V.; Pinto, F.; Lecumberri-Sanchez, P.; Schleicher, A.M. The imprint of hydrothermal fluids on trace-element contents in white mica and tourmaline from the Panasqueira W-Sn-Cu deposit, Portugal. *Mineral. Depos.* **2021**, *56*, 481–508. [CrossRef]
126. Borisova, A.Y.; Pichavant, M.; Polvé, M.; Wiedenbeck, M.; Freydier, R.; Candaudap, F. Trace element geochemistry of the 1991 Mt. Pinatubo silicic melts, Philippines: Implications for ore-forming potential of adakitic magmatism. *Geochim. Cosmochim. Acta* **2006**, *70*, 3702–3716. [CrossRef]
127. Herdianita, N.R.; Priadi, B. Arsenic and mercury concentrations at several geothermal systems in West Java, Indonesia. *ITB J. Sci.* **2008**, *40*, 1–14. [CrossRef]
128. Simmons, S.F.; Brown, K.L.; Tutolo, B.M. Hydrothermal transport of Ag, Au, Cu, Pb, Te, Zn and other metals and metalloids in New Zealand geothermal systems: Spatial patterns, fluid-mineral equilibria, and implications for epithermal mineralization. *Econ. Geol.* **2016**, *111*, 589–618. [CrossRef]
129. Greaney, A.T.; Rudnick, R.L.; Helz, R.T.; Gaschnig, R.M.; Piccoli, P.M.; Ash, R.D. The behavior of chalcophile elements during magmatic differentiation as observed in Kilauea Iki lava lake, Hawaii. *Geochim. Cosmochim. Acta* **2017**, *210*, 71–96. [CrossRef]
130. Cox, D. Chalcophile Element Processing and Distribution Beneath a Continental Volcanic Arc. Ph.D. Thesis, University of Birmingham, Birmingham, UK, 2019.
131. Li, Y.; Audétat, A. Partitioning of V, Mn, Co, Ni, Cu, Zn, As, Mo, Ag, Sn, Sb, W, Au, Pb, and Bi between sulfide phases and hydrous basanite melt at upper mantle conditions. *Earth Planet. Sci. Lett.* **2012**, *355*, 327–340. [CrossRef]
132. Hertogen, J.; Janssens, M.-J.; Palme, H. Trace elements in ocean ridge basalt glasses: Implications for fractionations during mantle evolution and petrogenesis. *Geochim. Cosmochim. Acta* **1980**, *44*, 2125–2143. [CrossRef]
133. Wang, Z.; Becker, H.; Liu, Y.; Hoffmann, E.; Chen, C.; Zou, Z.; Li, Y. Constant Cu/Ag in upper mantle and oceanic crust: Implications for the role of cumulates during the formation of continental crust. *Earth Planet. Sci. Lett.* **2018**, *493*, 25–35. [CrossRef]
134. Portnyagin, M.V.; Botcharnikov, R.E.; Yogodzinski, G.M.; Hoernle, K.; Garbe-Schönberg, D. Low Cu/Ag in continental crust and slab melts. In Proceedings of the Goldschmidt 2019 Abstract Volume, Barcelona, Spain, 18–23 August 2019.
135. König, S.; Münker, C.; Hohl, S.; Paulick, H.; Barth, A.R.; Lagos, M.; Pfander, J.; Büchl, A. The Earth's tungsten budget during mantle melting and crust formation. *Geochim. Cosmochim. Acta* **2011**, *75*, 2119–2136. [CrossRef]
136. Bali, E.; Keppler, H.; Audetat, A. The mobility of W and Mo in subduction zone fluids and the Mo-W-Th-U systematics of island arc magmas. *Earth Planet. Sci. Lett.* **2012**, *351–352*, 195–207. [CrossRef]
137. Hebert, L.B. (I) A Coupled Geochemical and Geodynamical Approach to Subduction Zone Modeling and (II) Development of Color in Greenish Quartz. Ph.D. Thesis, California Institute of Technology, Pasadena, CA, USA, 2008.
138. Ireland, T.J.; Arevalo, R., Jr.; Walker, R.J.; McDonough, W.F. Tungsten in Hawaiian picrites: A compositional model for the sources of Hawaiian lavas. *Geochim. Cosmochim. Acta* **2009**, *73*, 4517–4530. [CrossRef]
139. Arevalo, R., Jr.; McDonough, W.F. Tungsten geochemistry and implications for understanding the Earth's interior. *Earth Planet. Sci. Lett.* **2008**, *272*, 656–665. [CrossRef]
140. Bebout, G.E.; Barton, M.D. Metasomatism during subduction: Products and possible paths in the Catalina Schist, California. *Chem. Geol.* **1993**, *108*, 61–92. [CrossRef]
141. Bovay, T.; Rubatto, D.; Lanari, P. Pervasive fluid-rock interaction in subducted oceanic crust revealed by oxygen isotope zoning in garnet. *Contrib. Mineral. Petrol.* **2021**, *176*, 55. [CrossRef]
142. Jugo, P.; Luth, R.W.; Richards, J.P. An experimental study of the sulfur content in basaltic melts saturated with immiscible sulfide or sulfate liquids at 1300 °C and 1.0 GPa. *J. Petrol.* **2005**, *46*, 783–798. [CrossRef]
143. Peretti, A.; Dubessy, J.; Mullis, J.; Frost, B.R.; Trommsdorff, V. Highly reducing conditions during Alpine metamorphism of the Malenco peridotite (Sondrio, northern Italy) indicated by mineral paragenesis and H_2 in fluid inclusions. *Contrib. Mineral. Petrol.* **1992**, *112*, 329–340. [CrossRef]
144. Xiong, Q.; Griffin, W.L.; Huang, J.-X.; Gain, S.E.M.; Toledo, V.; Pearson, N.J.; O'Reilly, S.Y. Super-reduced mineral assemblages in "ophiolitic" chromitites and peridotites: The view from Mount Carmel. *Eur. J. Mineral.* **2017**, *29*, 557–570. [CrossRef]
145. Kadik, A.A.; Zharkova, E.V.; Rudashevsky, N.S. Redox conditions for the formation of Os-Ir-Ru-Pt and Fe-Pt minerals in ulramafic complexes. *Dokl. Earth Sci.* **1993**, *331*, 349–352.

146. Ariskin, A.A.; Fomin, I.S.; Zharkova, E.V.; Kadik, A.A.; Nikolaev, G.S. Redox conditions during crystallization of ultramafic and gabbroic rocks of the Yoko-Dovyren massif (based on the results of measurements of intrinsic fugacity of olivine). *Geochem. Internat.* **2017**, *55*, 595–607. [CrossRef]
147. Berdnikov, N.V.; Kepezhinskas, P.K.; Nevstruev, V.G.; Krutikova, V.O.; Konovalova, N.S. Magmatic native gold: Composition, texture, genesis, and evolution in the Earh's crust. *Russ. Geol. Geophys.* **2023**, *in press*.
148. Piccoli, F.; Hermann, J.; Pettke, T.; Connolly, J.A.D.; Kempf, E.D.; Vieira Duarte, J.F. Subducting serpentinites release reduced, not oxidized, aqueous fluids. *Sci. Rep.* **2019**, *9*, 19573. [CrossRef] [PubMed]
149. Evans, K.A.; Frost, B.R. Deserpentinization in subduction zones as a source of oxidation in arcs: A reality chechk. *J. Petrol.* **2021**, *62*, 1–32. [CrossRef]
150. Kendrick, M.A.; Honda, M.; Pettke, T.; Scambelluri, M.; Phillips, D.; Giuliani, A. Subduction zone fluxes of halogens and noble gases in seafloor and forearc serpentinites. *Earth Planet. Sci. Lett.* **2013**, *365*, 86–96. [CrossRef]
151. Fleet, M.E.; Wu, T.-W. Volatile transport of platinum-group elements in sulfide-chloride assemblages at 1000°. *Geochim. Cosmochim. Acta* **1993**, *57*, 3519–3531. [CrossRef]
152. Birner, S.K.; Warren, J.M.; Cottrell, E.; Davis, F.A.; Kelley, K.A.; Faloon, T.J. Forearc peridoties from Tonga arc record heterogeneous oxidation of the mantle following subduction initiation. *J. Petrol.* **2017**, *58*, 1755–1780. [CrossRef]
153. Brounce, M.N.; Kelley, K.A.; Cottrell, E. Variations in $Fe^{3+}/\sum Fe$ of Mariana arc basalts and mantle wedge fO_2. *J. Petrol.* **2014**, *55*, 2513–2536. [CrossRef]
154. König, S.; Münker, C.; Schuth, S.; Luguet, A.; Eliss Hoffmann, J.; Kuduon, J. Boninites as windows into trace element mobility in subduction zones. *Geochim. Cosmochim. Acta* **2010**, *74*, 684–704. [CrossRef]
155. Stoiber, R.E.; Rose, W.I., Jr. Fumarole incrustations at active Central American volcanoes. *Geochim. Cosmochim. Acta* **1974**, *38*, 495–516. [CrossRef]
156. Balassone, G.; Petti, C.; Mondillo, N.; Panikorovski, T.L.; de Gennaro, R.; Cappelletti, P.; Altomare, A.; Corriero, N.; Cangiano, M.; D'Orazio, L. Copper minerals at Vesuvius Volcano (Southern Italy): A mineralogical review. *Minerals* **2019**, *9*, 730. [CrossRef]
157. Zelenski, M.; Taran, Y.; Galle, B. High emission rate of sulfuric acid from Bezymianny volcano, Kamchatka. *Geophys. Res. Lett.* **2014**, *2015*, 7005–7013. [CrossRef]
158. Pekov, I.V.; Agakhanov, A.A.; Zubrova, N.V.; Koshlyakova, N.N.; Shchipalkina, N.V.; Sandalov, F.D.; Yapaskurt, V.O.; Turchkova, A.G.; Sidorov, E.G. Oxidizing-type fumaroles of the Tolbachik volcano, a mineralogical and geochemical unique. *Russ. Geol. Geophys.* **2020**, *61*, 675–688. [CrossRef]
159. Etschmann, B.E.; Liu, W.; Pring, A.; Grundler, P.V.; Tooth, B.; Borg, S.; Testemale, D.; Brewe, D.; Brugger, J. The role of Te(IV) and Bi(III) chloride complexes in hydrothermal mass transfer: An X-ray absorption spectroscopic study. *Chem. Geol.* **2016**, *425*, 37–51. [CrossRef]
160. Taran, Y.; Zelenski, M. Systematics of water isotopic composition and chlorine content in arc-volcanic gases. In *The Role of Volatiles in the Genesis, Evolution and Eruption of Arc Magmas*; Zellmer, G.F., Edmonds, M., Straub, S.M., Eds.; Special Publication 410; Geological Society: London, UK, 2014. [CrossRef]
161. Kishida, K.; Sohrin, Y.; Okamura, K.; Ishibashi, J. Tugnsten enriched in submarine hydrothermal fluids. *Earth Planet. Sci. Lett.* **2004**, *222*, 819–827. [CrossRef]
162. Liu, X.; Xiao, C. Wolframite solubility and precipitation in hydrothermal fluids: Insight from thermodynamic modeling. *Ore Geol. Rev.* **2020**, *117*, 103289. [CrossRef]
163. Manning, D.A.C.; Henderson, P. The behavior of tungsten in granitic melt-vapor systems. *Contrib. Mineral. Petrol.* **1984**, *86*, 286–293. [CrossRef]
164. Wang, X.-S.; Timofeev, A.; Williams-Jones, A.E.; Shang, L.-B.; Bi, X.-W. An experimental study of the solubility and speciaition of tungsten in NaCl-bearing aqueous solutions at 250, 300, and 350 °C. *Geochim. Comsochim. Acta* **2019**, *265*, 313–329. [CrossRef]
165. Wang, X.; Qiu, Y.; Chou, I.-M.; Zhang, R.; Li, G.; Zhong, R. Effects of pH and salinity on the hydrothermal transport of tungsten: Insights from in situ Raman spectroscopic characterization of K_2WO_4-NaCl-HCl-CO_2 solutions at temperatures up to 400 °C. *Geofluids* **2020**, *2020*, 2978984. [CrossRef]